Available online at www.sciencedirect.com

ScienceDirect

Advances in Space Research xxx (xxxx) xxx

ADVANCES IN SPACE RESEARCH (a COSPAR publication)

www.elsevier.com/locate/asr

Single track orbit determination analysis for low Earth orbit with approximated J2 dynamics

Jose M. Montilla [a,*,1], Jan A. Siminski [b,2], Rafael Vazquez [a,1]

[a] Universidad de Sevilla, Escuela Técnica Superior de Ingeniería, Camino de los Descubrimientos s.n, Sevilla 41092, Spain
[b] ESA/ESOC, Robert-Bosch-Str 5, Darmstadt 64293, Germany

Received 19 February 2024; received in revised form 10 September 2024; accepted 19 September 2024

Abstract

In the domain of Space Situational Awareness (SSA), the challenges related to orbit determination and catalog correlation are notably pronounced, exacerbated by data scarcity. This study introduces an initial orbit determination methodology that relies on data obtained from a single surveillance radar, with the need for fast algorithms within an operational context serving as the main design driver. The result is a linearized least-squares fitting procedure incorporating an analytically formulated approximation of the dynamics under the J_2 perturbation, valid for short-term propagation. This algorithm utilizes all available observables, including range-rate, distinguishing it from other similar methods. A significant contribution of this paper is the enhancement of estimation quality by incorporating information about the object's predicted orbital plane into the methodology, a method denoted as OPOD. The proposed methods are evaluated through a series of simulations against a classical range and angles fitting method (GTDS) to examine the effects of track length and measurement density on the quality of full state estimation, including the impact of using arcs that are too short. The OPOD methodology shows promising results throughout a wide range of scenarios.

Keywords: Initial orbit determination; Maneuver detection; Space situational awareness

1. Introduction

Over the last sixty years, human activities in space have significantly increased the number of orbiting objects (ESA, 2023), a concern heightened by the deployment of mega-constellations like Starlink and OneWeb. This congestion in low Earth orbit underscores the need for nations and space agencies to enhance tracking and cataloging efforts. Robust and efficient orbit determination (OD) algorithms are crucial in this context, playing a pivotal role in satellite tracking by swiftly identifying correlated tracks to maintain an accurate satellite database. The reliability of these algorithms is essential for Space Situational Awareness (SSA) and the safety of orbital operations.

Classical OD strategies involve an Initial Orbit Determination (IOD) phase to generate and initial estimate, which is later refined (Schutz et al., 2004), encompassing methods like those of Laplace, Gauss, and Gooding (Escobal, 1970; Gooding, 1993). These methods require measurements with at least six independent parameters to generate a six-parameter orbit, with the quality of the initial estimation benefiting from measurements originating from different observation arcs, referred to as tracks[3]. Generally, multiple

* Corresponding author.
E-mail addresses: jmontillag@us.es (J.M. Montilla), jan.siminski@esa.int (J.A. Siminski), rvazquez1@us.es (R. Vazquez).
[1] Aerospace Engineering and Fluid Mechanics Department, Spain.
[2] Space Debris Specialist, Space Debris Office, ESOC, Germany.

[3] A series of sequential observations delayed by seconds, which in turn are composed of a set of measurements (of different nature) at a common epoch.

https://doi.org/10.1016/j.asr.2024.09.035
0273-1177/

observation arcs lead to a *linkage* problem (Milani et al., 2004), where information from different tracks is correlated for proper OD (Milani et al. (2005);Ma et al. (2018)). This study aims to develop a reliable IOD method for single track radar measurements in the LEO regime, facilitating the automatic cataloging of uncorrelated tracks and subsequent maneuver detection within the context of the Spanish Space Surveillance and Tracking Surveillance Radar (S3TSR) (Gomez et al., 2019), and addressing the challenge of short arcs where arc length might be insufficient for existing methods (Tao et al., 2020). A significant contribution of this study is incorporating orbital plane data into the IOD process to enhance estimation quality.

The well-known range and angles method of the Goddard Trajectory Determination System (GTDS) (Long et al., 1989) is used as a reference for single track IOD in this work. However, this method is limited to inertial position information and cannot utilize the full set of observables provided by modern radars. Related to the method introduced here, Vallado and Carter (1998) apply a classical differential correction method for IOD with dense observation arcs and numerical propagation models. In contrast, this work focuses on leveraging analytical methods for scenarios with low-density radar tracks, where data scarcity is the primary challenge. The inclusion of extra information to aid in the estimation problem is an approach already present in other IOD methods proposed in the literature. The idea of initializing tracks with angles and angle-rates data, as explored in DeMars et al. (2012), is only suitable for optical-based sensors and not applicable to the LEO radar measurements used here. Other studies, such as Shang et al. (2018) and Zhang et al. (2019), involve multiple stations or very short tracks with extra radial measurements, which are beyond the scope of this work. For a more general review, see Pastor et al. (2021), which highlights the trade-off between speed and accuracy in combined Initial Orbit Determination and Orbit Determination methods.

Building on prior investigations (Montilla et al., 2023a; Montilla et al., 2023b), this work seeks to utilize all information from a single radar track, including range, range-rate, and line-of-sight data (azimuth and elevation). Consequently, we establish an IOD process based on radar-acquired data to estimate the satellite's full state. The use of attributables (Montilla et al., 2023a; Reihs et al., 2021) is replaced by a procedure that includes dynamics information, similar to the GTDS range and angles method (Siminski, 2016; Vananti et al., 2017). GTDS remains relevant for IOD, and it is a good alternative to classical 3 points methods such as Herrick-Gibbs (Kaushik, 2016), but leveraging all available observables, including range-rate data, should lead to better results. The unexpected need to incorporate Earth's flattening in short track orbital determination is a notable outcome explored in this study, given the relative importance of the J_2 perturbation compared to the main Keplerian term. For long-term non-Keplerian propagation, while approximated semi-analytical (Amato et al., 2019) or analytical methods (Martinusi et al., 2015) could be used, these are not suited for short track IOD applications. Numerical methods for uncertainty propagation (Hernando-Ayuso et al., 2023) also do not meet the computational efficiency requirements for real-time track association (Pastor et al., 2021).

The proposed method strikes a balance between error and speed, suitable for short propagations. The generalized equinoctial orbital elements in Baù et al. (2021) are used due to their explicit inclusion of potential-derived perturbations and slow evolution, making them ideal for short-term propagation through a Taylor expansion of the solution. This study produces the analytical time derivatives of these orbital elements, up to the fourth order, and calculates the error state transition matrix through the derivation of the resulting polynomial's coefficients. This is then used in a differential correction algorithm (Vallado, 2001) for IOD with the J_2 zonal harmonic included, along with an extended application involving past orbital data.

Thus, the main innovation of this work is the development of a comprehensive state estimation algorithm. This algorithm employs a basic linear least-squares method to directly fit radar observations, with state and uncertainty calculations performed using an analytical (approximated) J_2 propagator. Furthermore, the method is enhanced by incorporating expected orbital plane information—referred to as OPOD—into the process. In the LEO regime, this orbital plane can be reliably predicted based on prior estimates, even when considering potential maneuvers. The newly proposed methodologies are evaluated against a widely recognized orbit determination approach, demonstrating significant improvements in IOD for simulated tracks, while preserving the analytical framework essential for practical use.

The remainder of this paper is organized as follows. In Section 2, the problem and notation are defined. Section 3 describes the full state estimation algorithm first as a general linear least-squares method, then particularized to three different alternatives reliant only on data from a single radar track. This section includes an extra methodology that employs past orbital information to improve the estimation. Section 4 compiles detailed testing of the estimation methods based on simulated tracks. All methods are then applied to various scenarios that introduce variability in track length and measurement frequency. The document is closed with conclusions in Section 5. A includes most of the formulation needed in the presented work.

2. Problem statement and notation

This work seeks algorithms for IOD using a dynamical model to fit various satellite state-derived variables and radar observables from a single track (Fig. 1). It defines a radar station with known inertial position ($\boldsymbol{R}_r$), velocity ($\boldsymbol{V}_r$), and antenna orientation (given by the rotation matrix

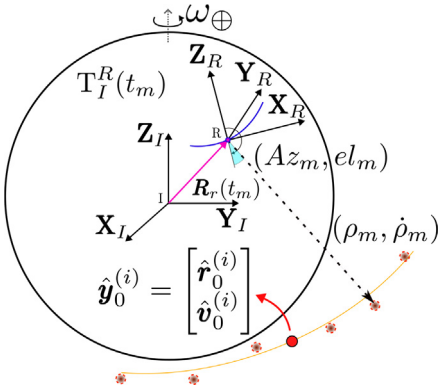

Fig. 1. The estimation problem from a single radar track is shown as iterative fitting of radar observables: range, azimuth, elevation, and range-rate $(\rho_m, Az_m, el_m, \dot{\rho}_m)$, creating a track of n observations from the same Resident Space Object.

T_I^R) for any required instant. The radar has a designated Field of Regard (FoR) characterized by a specific revisit time r_t. When a Resident Space Object (RSO) passes through the sensor's FoR, it generates a track composed of observations (also referred to as plots), which are sets of measurements taken at a common epoch t_m. Here, $m \in [1, n]$, where n is the number of individual plots. Typically, radar observables for LEO objects include range ρ_m, azimuth Az_m, elevation el_m, and range-rate $\dot{\rho}_m$. Each measurement has an error characterized by a known standard deviation, included in a covariance matrix C_{z_m} for the set, with potential correlations between different observables. Here the letter z denotes a general observed data point, typically a radar observable, but it can be any state derived quantity used for fitting. The notation is modified to $\hat{z}$ when said quantity is computed from the state that is being estimated in the fitting process.

It is assumed that the observation function $\boldsymbol{r}_m = \mathrm{OBS}_{fun}(\rho_m, Az_m, el_m)$ maps the radar observation of range and angles to an inertial position, which can then be treated as the measurement. This is needed for the GTDS method as it fits positions computed from the radar observables of range, azimuth and elevation. The covariance of such position measurement C_{r_m} is calculated from the original radar measurement uncertainty (C_{z_m}) using the Unscented Transform (UT) (Goff, 2015). The sigma points are reconstructed in inertial space to obtain the covariance matrix C_{r_m}, offering a more conservative uncertainty representation than the linear method (Siminski, 2016).

At the midpoint $t_0 = t_1 + (t_n - t_1)/2$ of the radar track, the satellite's state estimation $\hat{\boldsymbol{y}}_0 = [\hat{\boldsymbol{r}}_0\, \hat{\boldsymbol{v}}_0]$and its covariance C_y are computed. Note that $\hat{\boldsymbol{r}}_0$ and $\hat{\boldsymbol{v}}_0$ are the estimated inertial position and velocity in the Cartesian frame I. This approach requires calculating predicted measurements, $\hat{z}_m$, from the estimate $\hat{\boldsymbol{y}}_0$, necessitating the propagation of the orbital state to the instant t_m. The propagation step is encapsulated within $\hat{\boldsymbol{y}}_m = [\hat{\boldsymbol{r}}_m\, \hat{\boldsymbol{v}}_m] = \mathcal{P}(\hat{\boldsymbol{y}}_0, \Delta t_m)$, where $\Delta t_m = t_m - t_0$ is the propagation duration from the reference instant t_0, which is omitted [4]. The details of the propagation process will be discussed in Sections 3.1 and 3.3. The function $z = h(\boldsymbol{y}, t)$is defined to convert an inertial state $\boldsymbol{y}$ at an instant t to any observable z, allowing the computation of the predicted measurement $\hat{z}_m = h(\hat{\boldsymbol{y}}_m, t_m)$.

3. Iterative linearized least-squares fitting algorithm

This Section 3 reviews a general linear least-squares algorithm for any observable and propagation model. Section 3.1 adapts this algorithm to the GTDS, fitting position measurements with Keplerian dynamics. In Section 3.2, radar observables are fitted using a Kepler model, enhanced by a Taylor expansion for a more accurate computation of the derivatives. Section 3.3 applies generalized equinoctial orbital elements and a Taylor expansion for the inclusion of J_2 dynamics in short-track IOD. Finally, Section 3.4 proposes incorporating orbital plane information to enhance the orbit determination algorithm.

To maintain a broad scope, the fitting algorithm is derived from a general scalar observable z_m at time t_m with known standard deviation σ_m. The predicted measurement $\hat{z}_m = h(\hat{\boldsymbol{y}}_m, t_m)$ generally differs from the estimated state $\hat{\boldsymbol{y}}_0$, even without considering model inaccuracies in $\hat{\boldsymbol{y}}_m = \mathcal{P}(\hat{\boldsymbol{y}}_0, \Delta t_m)$. Thus, $z_m = \hat{z}_m + \xi_m$, where ξ_m is the residual. The goal is to minimize $\sum_{m=1}^{n}(w_m \xi_m)^2$, where $w_m = 1/\sigma_m$:

$$J_z = \min_{\hat{\boldsymbol{y}}_0} \sum_{m=1}^{n} (w_m \xi_m)^2. \tag{1}$$

A prerequisite is that the number of measurements must exceed the state dimension ($n > 6$). This leads to a nonlinear minimization problem, typically solved iteratively for efficiency. Assuming a good initial estimate of $\hat{\boldsymbol{y}}_0$, the predicted observable $\hat{z}_m$ is approximated at iteration i as a linearization around $\hat{z}_m^{(i)}$ for a variation $\Delta\hat{\boldsymbol{y}}_0^{(i)}$:

$$\begin{aligned} h(\hat{\boldsymbol{y}}_m, t_m) &\approx h\left(\mathcal{P}\left(\hat{\boldsymbol{y}}_0^{(i)}, \Delta t_m\right), t_m\right) + \left.\frac{\partial h}{\partial \hat{\boldsymbol{y}}_0}\right|_{(\hat{\boldsymbol{y}}_0^{(i)}, t_m)} \Delta\hat{\boldsymbol{y}}_0^{(i)} \\ &= h(\hat{\boldsymbol{y}}_m^{(i)}, t_m) + \left.\frac{\partial h}{\partial \boldsymbol{y}}\right|_{(\hat{\boldsymbol{y}}_m^{(i)}, t_m)} \left.\frac{\partial \mathcal{P}}{\partial \hat{\boldsymbol{y}}_0}\right|_{(\hat{\boldsymbol{y}}_0^{(i)}, \Delta t_m)} \Delta\hat{\boldsymbol{y}}_0^{(i)}. \end{aligned} \tag{2}$$

Considering all measurements $\boldsymbol{z} = [z_1, \cdots, z_n]^\intercal$, and the predicted measurements $\hat{\boldsymbol{z}}^{(i)} = \left[\hat{z}_1^{(i)}, \cdots, \hat{z}_n^{(i)}\right]^\intercal$ from $\hat{\boldsymbol{y}}_0^{(i)}$, the error $\Delta\boldsymbol{z}^{(i)} = \boldsymbol{z} - \hat{\boldsymbol{z}}^{(i)}$ is defined. The derivatives of the predicted value for the last iteration $\partial h/\partial \hat{\boldsymbol{y}}_0\big]_{(\hat{\boldsymbol{y}}_0^{(i)}, t_m)}$ are stacked in the matrix A to get the linear equation $\Delta\boldsymbol{z}^{(i)} = \mathrm{A}\,\Delta\boldsymbol{y}_0^{(i)} + \xi$. With this expression, the same minimization problem as in Eq. 1 can be solved as a linear least-squares problem:

[4] The propagation generally requires to specify the reference epoch t_0, but potential-based dynamics that go up to the second zonal harmonic does not depend on the reference instant, so only the total propagation time Δt_m is included in the formulation for brevity.

$$\begin{aligned}\Delta \boldsymbol{z}^{(i)} &= \mathrm{A}\,\Delta\hat{\boldsymbol{y}}_0^{(i)} + \xi,\\ J_z &= \min_{\Delta\hat{\boldsymbol{y}}_0^{(i)}} \boldsymbol{\xi}^{\intercal}\mathrm{W}\boldsymbol{\xi} = \min_{\Delta\hat{\boldsymbol{y}}_0^{(i)}} (\Delta\boldsymbol{z}^{(i)} - \mathrm{A}\,\Delta\hat{\boldsymbol{y}}_0^{(i)})^{\intercal}\mathrm{W}(\Delta\boldsymbol{z}^{(i)} - \mathrm{A}\,\Delta\hat{\boldsymbol{y}}_0^{(i)}),\\ \Delta\hat{\boldsymbol{y}}_0^{(i)} &= (\mathrm{A}^{\intercal}\mathrm{W}\mathrm{A})^{-1}(\mathrm{A}^{\intercal}\mathrm{W}\Delta\boldsymbol{z}^{(i)}),\end{aligned} \tag{3}$$

where $\mathrm{C}_y = (\mathrm{A}^{\intercal}\mathrm{W}\mathrm{A})^{-1}$ is the estimation covariance. Residual normalization is required, with $\mathrm{W} = \mathrm{C}_z^{-1}$ (inverted measurement covariance) and $\mathrm{C}_z = \mathrm{diag}\left(\sigma_1^2, \cdots, \sigma_n^2\right)$, for example. This differential correction approach simplifies the problem to iterations of a linear least-squares problem. While general convergence is not assured due to potential local minima, a close initial estimate offers a favorable speed-accuracy trade-off (Vallado, 2001). Iterations continue until the position displacement norm $|\,\Delta\hat{\boldsymbol{r}}_0^{(i)}\,|$ is below a threshold.

The propagation method $\mathcal{P}(\hat{\boldsymbol{y}}_0, \Delta t_m)$ and the relationship between spacecraft state and measurements in $h(\boldsymbol{y}, t)$ are particularized next with three analytical methods.

3.1. Keplerian fitting of non-weighted Cartesian position - GTDS

The GTDS range and angles method (Siminski, 2016; Vananti et al., 2017) is a specific case of the general algorithm from Section 3. This method fits measurements in inertial position, represented by $\boldsymbol{r}_m$ at each instant t_m, so the vector of all measurements is $\boldsymbol{z} = \left[\boldsymbol{r}_1^{\intercal}, \boldsymbol{r}_2^{\intercal}, \cdots, \boldsymbol{r}_n^{\intercal}\right]^{\intercal}$.

Predicted measurements $\hat{\boldsymbol{r}}_m$ are an explicit function of the propagated estimation $\hat{\boldsymbol{y}}_m$, given by $\hat{\boldsymbol{r}}_m = h(\hat{\boldsymbol{y}}_m, t_m)$. The propagation function $\mathcal{P}(\hat{\boldsymbol{y}}_0, \Delta t)$ ensures Keplerian dynamics. This is achieved using the universal variable χ, which is applicable to all orbit types and allows computation of the f and g Kepler functions, yielding the propagated state as a linear combination of the initial conditions:

$$\hat{\boldsymbol{y}}_m = \mathcal{P}(\hat{\boldsymbol{y}}_0, \Delta t_m) = \begin{bmatrix}\hat{\boldsymbol{r}}(\hat{\boldsymbol{y}}_0, \Delta t_m)\\ \hat{\boldsymbol{v}}(\hat{\boldsymbol{y}}_0, \Delta t_m)\end{bmatrix} = \begin{bmatrix} f(\hat{\boldsymbol{r}}_0, \hat{\boldsymbol{v}}_0, \Delta t_m)\hat{\boldsymbol{r}}_0 + g(\hat{\boldsymbol{r}}_0, \hat{\boldsymbol{v}}_0, \Delta t_m)\hat{\boldsymbol{v}}_0\\ \dot{f}(\hat{\boldsymbol{r}}_0, \hat{\boldsymbol{v}}_0, \Delta t_m)\hat{\boldsymbol{r}}_0 + \dot{g}(\hat{\boldsymbol{r}}_0, \hat{\boldsymbol{v}}_0, \Delta t_m)\hat{\boldsymbol{v}}_0\end{bmatrix}. \tag{4}$$

The details for computing f and g are provided in *Algorithm 8* of Vallado (2001). For the iterative method, the predicted position $\hat{\boldsymbol{r}}(\hat{\boldsymbol{y}}_0, \Delta t)$ must be linearized around $\hat{\boldsymbol{r}}_0^{(i)}$ and $\hat{\boldsymbol{v}}_0^{(i)}$ for variations $\Delta\hat{\boldsymbol{r}}_0^{(i)}$ and $\Delta\hat{\boldsymbol{v}}_0^{(i)}$:

$$\begin{aligned}\hat{\boldsymbol{r}}(\hat{\boldsymbol{r}}_0, \hat{\boldsymbol{v}}_0) &\approx \hat{\boldsymbol{r}}(\hat{\boldsymbol{r}}_0^{(i)}, \hat{\boldsymbol{v}}_0^{(i)}) + \tfrac{\partial\hat{\boldsymbol{r}}}{\partial\hat{\boldsymbol{r}}_0}\rfloor^{(i)}\Delta\hat{\boldsymbol{r}}_0^{(i)} + \tfrac{\partial\hat{\boldsymbol{r}}}{\partial\hat{\boldsymbol{v}}_0}\rfloor^{(i)}\Delta\hat{\boldsymbol{v}}_0^{(i)},\\ \tfrac{\partial\hat{\boldsymbol{r}}}{\partial\hat{\boldsymbol{r}}_0}\rfloor^{(i)} &= f^{(i)}\tfrac{\partial\hat{\boldsymbol{r}}_0}{\partial\hat{\boldsymbol{r}}_0} + \hat{\boldsymbol{r}}_0^{(i)}\tfrac{\partial f}{\partial\hat{\boldsymbol{r}}_0}\rfloor^{(i)} + \hat{\boldsymbol{v}}_0^{(i)}\tfrac{\partial g}{\partial\hat{\boldsymbol{r}}_0}\rfloor^{(i)},\\ \tfrac{\partial\hat{\boldsymbol{r}}}{\partial\hat{\boldsymbol{v}}_0}\rfloor^{(i)} &= g^{(i)}\tfrac{\partial\hat{\boldsymbol{v}}_0}{\partial\hat{\boldsymbol{v}}_0} + \hat{\boldsymbol{r}}_0^{(i)}\tfrac{\partial f}{\partial\hat{\boldsymbol{v}}_0}\rfloor^{(i)} + \hat{\boldsymbol{v}}_0^{(i)}\tfrac{\partial g}{\partial\hat{\boldsymbol{v}}_0}\rfloor^{(i)}.\end{aligned} \tag{5}$$

The dependence over Δt has been dropped for conciseness. The GTDS method simplifies this by setting $\partial f/\partial\boldsymbol{r}_0 = \partial f/\partial\boldsymbol{v}_0 = \partial g/\partial\boldsymbol{r}_0 = \partial g/\partial\boldsymbol{v}_0 = \boldsymbol{0}^{\intercal}$, reducing the derivatives to $\partial\hat{\boldsymbol{r}}/\partial\hat{\boldsymbol{r}}_0\rfloor^{(i)} \approx f^{(i)}\mathrm{I}_3$and $\partial\hat{\boldsymbol{r}}/\partial\hat{\boldsymbol{v}}_0\rfloor^{(i)} \approx g^{(i)}\mathrm{I}_3$. The matrix I_3 is the identity matrix of order 3. Applying this technique to the linearization of the predicted position results in:

$$\begin{aligned}\hat{\boldsymbol{r}}(\hat{\boldsymbol{r}}_0, \hat{\boldsymbol{v}}_0) &\approx \hat{\boldsymbol{r}}(\hat{\boldsymbol{r}}_0^{(i)}, \hat{\boldsymbol{v}}_0^{(i)}) + \tfrac{\partial\hat{\boldsymbol{r}}}{\partial\hat{\boldsymbol{r}}_0}\rfloor^{(i)}\Delta\hat{\boldsymbol{r}}_0^{(i)} + \tfrac{\partial\hat{\boldsymbol{r}}}{\partial\hat{\boldsymbol{v}}_0}\rfloor^{(i)}\Delta\hat{\boldsymbol{v}}_0^{(i)}\\ &\approx f^{(i)}\hat{\boldsymbol{r}}_0^{(i)} + g^{(i)}\hat{\boldsymbol{v}}_0^{(i)} + f^{(i)}\Delta\hat{\boldsymbol{r}}_0^{(i)} + g^{(i)}\Delta\hat{\boldsymbol{v}}_0^{(i)}\\ &= f^{(i)}(\hat{\boldsymbol{r}}_0^{(i)} + \Delta\hat{\boldsymbol{r}}_0^{(i)}) + g^{(i)}(\hat{\boldsymbol{v}}_0^{(i)} + \Delta\hat{\boldsymbol{v}}_0^{(i)}) = f^{(i)}\hat{\boldsymbol{r}}_0^{(i+1)} + g^{(i)}\hat{\boldsymbol{v}}_0^{(i+1)}.\end{aligned} \tag{6}$$

Thus, the predicted measurement at t_m can be expressed as:

$$\begin{aligned}\hat{\boldsymbol{r}}_m = \hat{\boldsymbol{r}}(\hat{\boldsymbol{r}}_0, \hat{\boldsymbol{v}}_0, \Delta t_m) &\approx f_m^{(i)}\mathrm{I}_3\hat{\boldsymbol{r}}_0^{(i+1)} + g_m^{(i)}\mathrm{I}_3\hat{\boldsymbol{v}}_0^{(i+1)}\\ &= \begin{bmatrix} f_m & 0 & 0 & g_m & 0 & 0\\ 0 & f_m & 0 & 0 & g_m & 0\\ 0 & 0 & f_m & 0 & 0 & g_m\end{bmatrix}^{(i)}\begin{bmatrix}\hat{\boldsymbol{r}}_0^{(i+1)}\\ \hat{\boldsymbol{v}}_0^{(i+1)}\end{bmatrix}.\end{aligned} \tag{7}$$

Using the form in Eq. (7), the vector of predicted positions ($\hat{\boldsymbol{z}}$) can be expressed by linearly combining the estimation $\hat{\boldsymbol{y}}_0^{(i+1)}$ with the Kepler functions at the corresponding instants. The position residuals in $\boldsymbol{z} = \mathrm{A}\hat{\boldsymbol{y}}_0^{(i+1)} + \boldsymbol{\xi}$ are thus an explicit linear function of the estimation $\hat{\boldsymbol{y}}_0^{(i+1)}$. By solving the linear least-squares in Eq. (3) with W being the identity matrix (non-weighted), the solution is given by:

$$\begin{aligned}\hat{\boldsymbol{y}}_0^{(i+1)} &= (\mathrm{A}^{\intercal}\mathrm{A})^{-1}\mathrm{A}^{\intercal}\boldsymbol{z} = \mathrm{H}\,\boldsymbol{z},\\ \mathrm{C}_y &= \mathrm{H}\mathrm{C}_r\mathrm{H}^{\intercal},\ \text{where}\mathrm{C}_r = \mathrm{diag}(\mathrm{C}_{r_1}, \cdots, \mathrm{C}_{r_n}),\end{aligned} \tag{8}$$

is that of the GTDS method. Emphasis has to be placed on the choice of not weighting position residuals despite the availability of an uncertainty characterization. The result is a fit that minimizes errors in all directions equally. The covariance of the estimation is computed from the matrix $\mathrm{H} = (\mathrm{A}^{\intercal}\mathrm{A})^{-1}\mathrm{A}^{\intercal}$ as a linear approximation after the estimation is computed (in the last iteration). For a more compact form of the solution to Eq. (8), see Siminski (2016).

3.2. Keplerian fitting of radar observables - KEP

This method modifies GTDS by fitting measurements directly with Keplerian dynamics, incorporating range-rate information. The measurement vector includes all observables directly, denoted as $\boldsymbol{z} = [\rho_1, Az_1, el_1, \dot{\rho}_1, \ldots, \rho_n, Az_n, el_n, \dot{\rho}_n]^{\intercal}$. The function $h(\boldsymbol{y}, t)$ for these measurements, as well as the derivatives $\partial h/\partial\boldsymbol{y}$, is found in the A.1. Incorporating range-rate requires predicted position and velocity, computed via $\dot{f}$ and $\dot{g}$ functions, as shown in Eq. (4).

The computation of $\partial h/\partial\hat{\boldsymbol{y}}_0$, see Eq. (2), requires the predicted full state derivatives, $\partial\mathcal{P}/\partial\hat{\boldsymbol{y}}_0$. The position part is found in Section 3.1, Eq. (5). Predicted velocity derivatives are also required, but the GTDS approximation neglecting Kepler function derivatives is unsuitable here. An analytical approximation for $f, g, \dot{f}$, and $\dot{g}$ derivatives has been employed using a fourth order Taylor expansion around $\hat{\boldsymbol{r}}_0$ and $\hat{\boldsymbol{v}}_0$. Detailed expressions are omitted for brevity but can be found in Vallado (2001). Thus, the element $\partial\mathcal{P}/\partial\hat{\boldsymbol{y}}_0$ can be computed at each Δt_m with the necessary precision.

With $\partial h/\partial\hat{\boldsymbol{y}}_0$ computed, all elements to solve the linear least-squares problem in Eq. (3) are available. Errors $\Delta\boldsymbol{z}^{(i)}$ are computed using the propagated estimates $\hat{\boldsymbol{y}}_m^{(i)}$,

via Eq. (4), evaluated in the observation function (A.1). This is the second analytical method, denoted simply as KEP.

3.3. J_2 fitting of radar observables - KEP + J2

A third algorithm incorporating J_2 perturbation has been developed. While analytical methods exist for oblate planet perturbations, they often sacrifice precision and are valid only for specific eccentricity ranges (Martinusi et al., 2015). This work uses an solution valid for short time spans, based on the generalized equinoctial orbital elements (GEqOE) described in Baù et al. (2021).

3.3.1. GEqOE formulation

Given a perturbation force derivable from a potential energy $\mathcal{U}$, the GEqOE incorporate the perturbing potential in their definition, generalizing the classical equinoctial elements (Broucke and Cefola, 1972). This formulation yields the generalized semi-major axis (a) and Laplace vector ($\mu \boldsymbol{g}$), defining a non-osculating ellipse in the orbital plane. The elements p_1 and p_2 are projections of $\boldsymbol{g}$ along in-plane axes, while Kepler's equation is written using the generalized mean longitude $\mathcal{L}$:

$$\mathcal{L} = \mathcal{K} + p_1 \cos\mathcal{K} - p_2 \sin\mathcal{K}, \tag{9}$$

where $\mathcal{K}$ is the generalized eccentric longitude. The generalized mean motion v derives from the total energy, which includes $\mathcal{U}$. Elements q_1 and q_2 (equal to the classical p and q) complete the GEqOE set $\boldsymbol{\chi} = [v, p_1, p_2, q_1, q_2, \mathcal{L}]$. The first-order time derivatives of these elements are explicit functions of $\mathcal{U}$ and other forces contained in $\boldsymbol{P}$ (drag, luni-solar perturbations,...). This general formulation can be simplified to include the J_2 perturbation only:

$$\begin{aligned}
\dot{v} &= 0,\\
\dot{p}_1 &= p_2\left(\tfrac{h-c}{r^2} - I\hat{z}\right) - \tfrac{1}{c}\left(\tfrac{X}{a} + 2p_2\right)\mathcal{U},\\
\dot{p}_2 &= p_1\left(I\hat{z} - \tfrac{h-c}{r^2}\right) + \tfrac{1}{c}\left(\tfrac{Y}{a} + 2p_1\right)\mathcal{U},\\
\dot{q}_1 &= -I\tfrac{Y}{r},\\
\dot{q}_2 &= -I\tfrac{X}{r},\\
\dot{\mathcal{L}} &= v + \tfrac{h-c}{r^2} - I\hat{z} - \tfrac{1}{c}\left[\tfrac{1}{\alpha} + \alpha\left(1 - \tfrac{r}{a}\right)\right]\mathcal{U}.
\end{aligned} \tag{10}$$

Here, v is constant since the only perturbation is conservative and therefore the total energy is conserved. Some definitions needed for the use of the GEqOE can be found in the A.4.2. Algorithms 1,2 in the A.7 convert between inertial position/velocity and GEqOE.

Numerical integration of Eq. (10) requires the X and Y values. Given initial GEqOE values, the generalized Kepler's equation is solved, see Eq. (9), with the output $\mathcal{K}$ used then to compute r, X, and Y:

$$\begin{aligned}
r &= a(1 - p_1\sin\mathcal{K} - p_2\cos\mathcal{K}),\\
X &= a\left[\alpha p_1 p_2 \sin\mathcal{K} + (1 - \alpha p_1^2)\cos\mathcal{K} - p_2\right],\\
Y &= a\left[\alpha p_1 p_2 \cos\mathcal{K} + (1 - \alpha p_2^2)\sin\mathcal{K} - p_1\right].
\end{aligned} \tag{11}$$

In Baù et al. (2021), GEqOE's slower evolution is reported to reduce numerical integration error. Applying a Taylor expansion in this state representation is thus an interesting alternative. This section aims to derive an analytical solution for IOD.

3.3.2. Taylor expansion in GEqOE

A special notation is introduced to differentiate the ODEs in Eq. (10). The function $\not{f}_s = 1/s$ simplifies the application of the chain rule in derivation when an element is dividing. For example, $\dot{r} = \mu/c(p_2 \sin L - p_1 \cos L)$, expressed with the true longitude L, can be rewritten as $\dot{r} = \mu \not{f}_c r_{pl}$. The time derivative becomes $\ddot{r} = \mu(\dot{\not{f}}_c r_{pl} + \not{f}_c \dot{r}_{pl})$, requiring $\dot{\not{f}}_s = -\dot{s}/s^2$. A function that computes time derivatives of $\not{f}_s$ has been implemented, taking the vector $[s, \dot{s}, \ddot{s}, \cdots]$ as input (see A.2). The function $\not{g}_s = s\dot{s}$ is also introduced, appearing when differentiating s^2 (see A.3 for time derivatives of $\not{g}_s$).

First-order derivatives of the Taylor expansion involve evaluating the ODEs. For higher orders, elements in Eq. (10) are split into easily derivable parts, as shown in Eq. (A.9) for $\hat{z}$. This method compacts the equations of motion, see Eq. A.6. Full derivation up to fourth order and symbol definitions are given in A.4.

After computing the derivatives at the epoch, a Taylor expansion propagates the state vector $\boldsymbol{\chi}(\boldsymbol{\chi}_0, \Delta t_m) = [v, p_1, p_2, q_1, q_2, \mathcal{L}]^\intercal$ to all Δt_m, which is then converted to Cartesian using Algorithm 2. The analytical derivative of $\boldsymbol{\chi}(\boldsymbol{\chi}_0, \Delta t_m)$ with respect to $\boldsymbol{\chi}_0$ is computed to obtain $\frac{\partial \boldsymbol{\chi}}{\partial \boldsymbol{\chi}_0}$. This involves differentiating the functions $\not{f}_s$ and $\not{g}_s$ (and their time derivatives) with respect to a generic orbital element (see A.5). The resulting analytical derivatives have been validated using Taylor differential algebra with Hipparchus.

To convert between GEqOE and Cartesian states (see Algorithms 1 and 2) and derivatives, the Jacobians of both transformations, RV2GEQOE $\left(\frac{\partial \boldsymbol{\chi}}{\partial \boldsymbol{X}}\right)$ and GEQOE2RV $\left(\frac{\partial \boldsymbol{X}}{\partial \boldsymbol{\chi}}\right)$, are used (Baù et al., 2021). Cartesian derivatives are obtained by multiplying the Jacobians evaluated at the correct instant:

$$\frac{\partial \boldsymbol{X}}{\partial \boldsymbol{X}_0} = \frac{\partial \boldsymbol{X}}{\partial \boldsymbol{\chi}}\bigg|_t \left(\frac{\partial \boldsymbol{\chi}}{\partial \boldsymbol{\chi}_0}\right) \frac{\partial \boldsymbol{\chi}}{\partial \boldsymbol{X}}\bigg|_{t_0}, \tag{12}$$

validated by numerically integrating the variational equations with the J_2 perturbation added. This completes the method, referred to as KEP + J2.

3.4. Adding extra information: Orbital Plane-based Orbit Determination - OPOD

Precise initial orbit determination using a single radar track is challenging due to the scarcity of data. This section presents an alternative approach, Orbital Plane-based Orbit Determination (OPOD), to improve the quality and

reliability of the estimation by exploiting information from a known past state. The key assumption is that for LEO objects maneuvers are usually performed to maintain altitude and do not significantly affect the orbital plane, as changing the inclination (i) or right ascension of the ascending node (RAAN, Ω) is expensive.

In OPOD, the orbital plane is predicted from the known past orbit with relatively high precision, assuming that process noise (primarily drag uncertainty) does not directly affect the i and Ω prediction, even in the presence of maneuvers. The predicted orbital plane information is then added as virtual measurements at the radar epoch (t_0), independent of the measurements, to constrain the region of inertial space that the spacecraft could occupy at that instant. This reduces the uncertainty of the estimation, with the level of improvement depending on the uncertainty assigned to these virtual measurements.

It is important to note that OPOD does not decouple plane attitude estimation from the in-plane estimation, nor does it assume the plane to be deterministic or even constant. The state is still estimated using the same least-squares fitting approach, considering all measurements (radar track and virtual orbital plane) through the dynamical model. The addition of orbital plane information at the radar epoch simply provides extra constraints to improve the estimation accuracy. In fact, when the fitting dynamics include the J_2 perturbation, even if the orbital plane is assumed partially known at a given instant it does change along the track.

The measurement function $h(\boldsymbol{y}, t)$ for these new observables, as well as the analytical derivative with respect to the Cartesian state $\partial h/\partial \boldsymbol{y}$ are in the A.6. The addition of these virtual measurements can be applied to either the KEP or KEP + J2 fitting of radar measurements, but not the GTDS method as it only works with position information.

4. Simulated results

For this section, simulations of the satellite's trajectory and radar measurements are used to evaluate IOD methods'performance. Orekit (Maisonobe et al., 2010) handles all high-fidelity satellite dynamics and radar simulations, see Section 4.1. Section 4.2 presents preliminary testing of radar-only IOD methods, establishing baseline performance and track length dependency. Section 4.3 tests the orbital-plane enhanced method (OPOD), showing the impact of adding orbital plane information and uncertainty even in presence of maneuvers. Section 4.4 details the simulated testing methodology and scenarios, generating track data for Section 4.5, where a k^2 metric tests uncertainty characterization of estimation errors.

4.1. Dynamical modeling and radar characterization

For IOD methods relying on sensor data, the testing involves simulating "real" satellite trajectories and generating radar tracks. The OPOD algorithm, reliant upon predicted orbital plane, requires two distinct dynamics. Table 1 lists the dynamical models for numerical simulations. The main difference between *True* and *Prediction* dynamics is the atmosphere model and harmonics degree. NRLMSISE-00 (Picone et al., 2002) and DTM-2000 (Bruinsma et al., 2003) models account for tabulated solar weather data, differing in order to reflect atmospheric uncertainty in practice.

High-fidelity (HF) and low-fidelity (LF) satellite models are defined in Tables 2 and 3, respectively. HF satellites are defined by its dimensions, solar array area (A_s) and orientation in local axis (A_x), drag (C_D), absorption (a_c) and reflection (r_c) coefficients. LF satellites use a simple spherical drag model. HF models pair with True dynamics for simulating trajectories and radar measurements, while LF models use Prediction dynamics for orbital plane predictions.

Satellites named for real-world equivalents vary in orbit type: Sentinel-1A (700 km), Swarm-C (430 km), Starlink-1 and 2 (540 km). Table 4 provides initial conditions for simulated scenarios, generating diverse radar track lengths. Only Sentinel-1A and Swarm-C have corresponding LF models for OPOD testing. Other IOD methods (Sections 3.1, 3.2, 3.3) are tested on all satellites.

Simulations use Orekit (Maisonobe et al., 2010) for dynamics and measurement generation. Orekit handles sensor measurements, taking into account reflection time and ionospheric delay. Measurement generation adds noise with constant covariance and no biases, a simple model suitable for limited orbital regimes. The radar's uncertainty characterization is assumed known for estimation. Table 5

Table 1
The two dynamical models defined, one for the true trajectory and the other for the prediction. SRP stands for Solar Radiation pressure.

Model	Earth harmonics	Atmosphere	Sun	Moon	SRP
True	[150, 150]	DTM-2000	yes	yes	yes
Prediction	[40, 40]	NRLMSISE-00	yes	yes	yes

Table 2
Parameters defining the realistic satellites Sentinel-1A, Swarm-C and Starlink-1/2 using Orekit's *BoxAndSolarArraySpacecraft* force model class.

HF Satellite	m (kg)	x_l (m)	y_l (m)	z_l (m)	A_s (m^2)	A_x [-]	C_D [-]	a_c [-]	r_c [-]
Sentinel-1A	2270	1.02	1.34	3.2	25.46	y	1.5	0.8	0.5
Swarm-C	440	1.3	8	0.9	0.1	y	0.95	0.9	0.5
Starlink-1	1250	2.8	2.3	0.3	25.2	z	0.9	0.9	0.5
Starlink-2	800	2.5	2	0.2	20	z	0.92	0.9	0.5

Table 3
Parameters defining the low fidelity satellites Sentinel-1A$_1$ and Swarm-C$_1$ using Orekit's isotropic drag and radiation force model classes. These parameters are: mass, drag cross section, drag coefficient, solar radiation cross section and reflection coefficient.

LF Satellite	m (kg)	S (m^2)	C_D [-]	SRP_s (m^2)	r_c [-]
Sentinel-1A$_1$	2200	9.5	2	10	1.4
Swarm-C$_1$	420	4	2.56	4	1.4

specifies radar parameters for three different stations used separately in the simulations, enriching track length variability and data density across scenarios. Radar location is given by its geodetic coordinates longitude (λ), latitude (ϕ) and height (h). The radar antenna orientation is given by 3 consecutive rotations $(\varphi_x, \varphi_y, \varphi_z)$ around its local x, y, and z axes. Initially, it is parallel to the XY plane of the topocentric frame. The field of regard (FoR) is defined by scanning angles U and V, limited in both positive and negative directions, forming a volume outside two intersecting concentric cones. Radar 1 is a simulation of S3TSR (Gomez et al., 2019), and some of its characteristics have been omitted for confidentiality. Radars 2 and 3 have been defined for testing purposes, with similar characteristics to the S3TSR simulation. In all cases radar characterization is assumed perfectly known.

4.2. Preliminary testing of the IOD algorithms

With the simulation and fitting methods in place (see Section 3), a controlled test is needed to compare them. Understanding each method's limitations helps to interpret the estimation statistics (see Section 4.5.1). The approach involves applying the three IOD algorithms to a single radar track using only radar data. To study the effect of track length on estimation accuracy and uncertainty, a long track is shortened incrementally by removing measurements from the ends and repeating the fitting.

The longest track from Radar 3, simulating Sentinel-1A over 4 days, is chosen. It consists of 72 measurements spanning 284 s.

4.2.1. Fitting of noiseless measurements

First, it is essential to consider the true values of the measurements, rather than the noisy ones, to emphasize the base limitations of each method. Propagating the true position and velocity at the epoch of the test track with Kepler dynamics results in position errors on the order of 100 meters and range errors over 50 m (Fig. 2, Left). This trajectory coincides with the true one at the epoch, yet the Kepler model incurs range errors an order of magnitude greater than the radar measurements'uncertainty.

Applying the GTDS algorithm to the true position measurements results in the estimation with errors shown in Fig. 2 (Center). The square sum of errors ($\boldsymbol{\xi}^\intercal\boldsymbol{\xi}$) is minimized, and without weights, the position errors are lower on average along the complete trajectory, but not necessarily the range errors.

In Fig. 2 (Right), the position fitting is done by minimizing $\boldsymbol{\xi}^\intercal \mathrm{W} \boldsymbol{\xi}$, with $\mathrm{W} = \mathrm{C}_r^{-1}$. The position covariance computed with an UT has greater variance in the range direction than the original measurement space uncertainty, but it is still a thin disk in Cartesian space. The estimation error is on the order of a kilometer, while still fitting exact position values. The increased weight of the error in the range direction forces lower residuals in that direction, while residuals in perpendicular directions are less relevant, especially for measurements further from the radar. The problem lies in pairing Kepler dynamics with a strongly directional weighting, as the model cannot maintain low range residuals for such a long pass (Fig. 2, Left), so the fitting algorithm has to change the trajectory considerably.

When fitting true radar observables directly with a Kepler model (see Section 3.2), the problem exacerbates (Fig. 3, Left), with an epoch position error of 1.5 km. This is due to the range being even more relevant to the weighting and the addition of a range-rate constraint with very low uncertainty.

The approximated J_2 propagator (Section 3.3.2) is tested up to the fourth term of the Taylor expansion (see Table 6 for constants). Absolute position errors compared to numerical propagation are below 1 cm for a 100-s propagation (Fig. 4). Fig. 3 (Center) shows the errors when the true state is propagated from the epoch using the J_2 propagator, with range residuals barely over 1 meter at worst. Consequently, the radar observables fitting is much more similar to the original trajectory (Fig. 3, Right), indicating this might be superior to GTDS if only position errors are considered.

Fig. 5 compares the methods for different track lengths with noiseless measurements, representing the error at the epoch when the fitted trajectory gets shorter as measurements are extracted in pairs from the sides of the test track. A shorter trajectory can be better fitted with simplified dynamics. The KEP fit of measurements is the worst of

Table 4
Initial condition (I.C.) for the reference orbit defined for the scenarios in Table 8, in Cartesian coordinates (Earth EME2000 inertial frame). The initial epoch t_0 is at 00:00:00 UT.

I.C.	x (km)	y (km)	z (km)	v_x (km/s)	v_y (km/s)	v_z (km/s)	t_0
S1A-1	1459.975	436.989	−6916.264	−3.8952	−6.282	−1.219	01/05/2022
SWC-1	254.597	−241.108	6792.396	7.151	2.655	−0.1728	06/07/2020
SRL-1	4970.721	3941.433	602.664	−4.458	4.973	4.244	27/08/2023
SRL-2	5030.115	3838.607	754.660	−4.040	4.249	5.315	27/08/2023

Table 5
Complete characterization of the radar stations used for the simulated testing.

Name	Radar 1	Radar 2	Radar 3
(λ, ϕ) (°)	$(-5.59, 37.17)$	$(22.3, 78.49)$	$(175.68, -37.86)$
h (m)	142.32	22.14	36.2
$(\varphi_x, \varphi_y, \varphi_z)$ (°)	-	$(40, 0, 0)$	$(30, 0, 0)$
(U_{min}, U_{max}) (°)	-	$(-30, 30)$	$(-20, 20)$
(V_{min}, V_{max}) (°)	-	$(-20, 20)$	$(-45, 45)$
σ_ρ (m)	7	6.5	6.5
$\sigma_{\dot\rho}$ (m/s)	0.4	0.35	0.35
σ_{Az} (°)	0.3	0.25	0.25
σ_{el} (°)	0.2	0.15	0.15
$\xi_{Az,el}$	0.043	0.043	0.043
r_t (s)	7	4	4

the three, but very short tracks do not degrade as much in terms of estimated position bias. The KEP + J2 fit with J_2 perturbation seems to be the best in this regard, but GTDS has a small advantage in velocity errors, which can only occur under the condition of perfect position measurements. Since the GTDS method assigns equal weight to all residuals, errors stemming from the basic dynamics are effectively averaged out.

4.2.2. Fitting of noisy measurements

When noise is introduced (Fig. 6) and results are averaged over multiple fittings, there is little difference between the methods for tracks shorter than 100 s in terms of average position error. GTDS has a slight disadvantage in

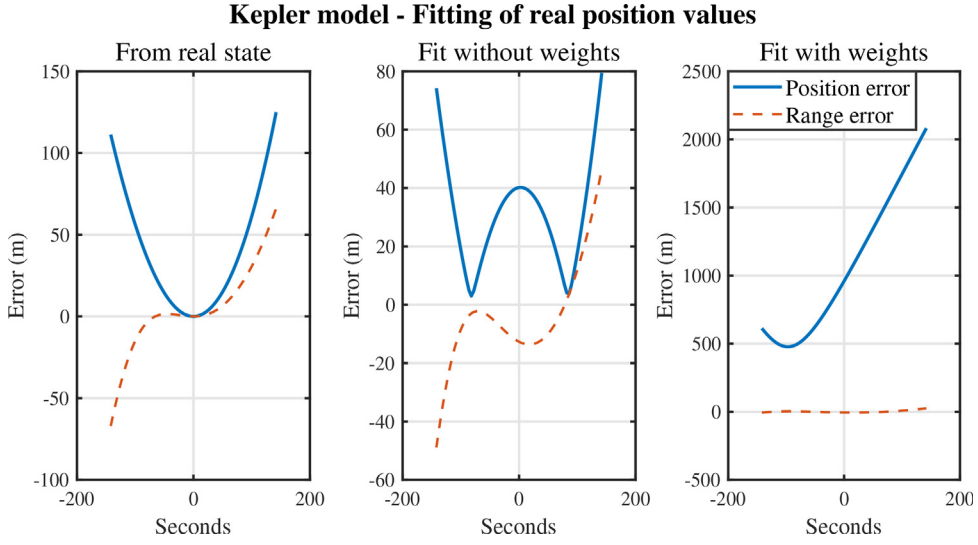

Fig. 2. Kepler-based trajectories vs. true positions for a 284-s radar track. Range error is the position error projected along the satellite-radar vector. Left: Trajectory starting from the true state at epoch. Center: Fitting of true positions without weights. Right: Fitting of true positions with weights.

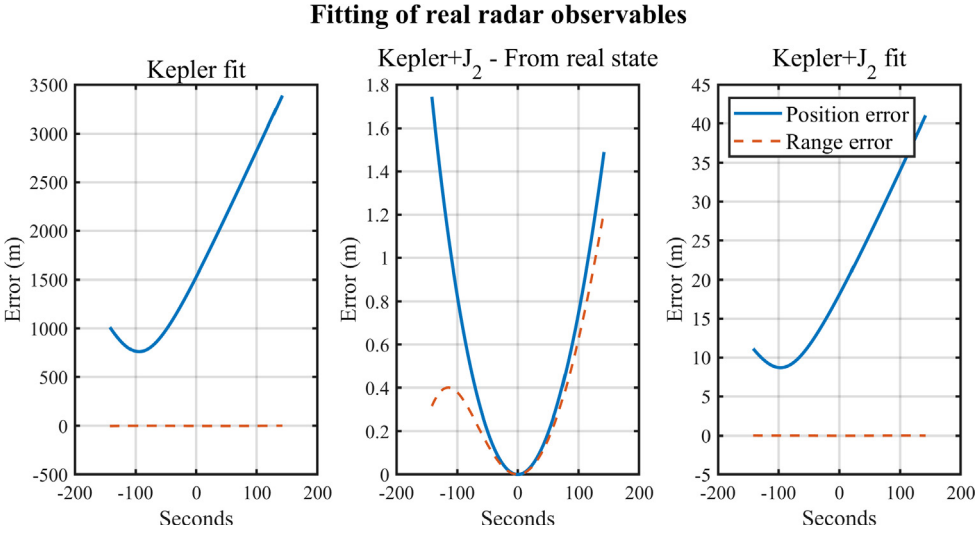

Fig. 3. Position and range errors using true radar measurements, including range-rate, for the same sample track as in Fig. 2. Left: Kepler dynamics fitting. Center: Analytical J_2 propagation from the true state at t_0. Right: Analytical fitting with J_2.

velocity errors for the first half of the interval, due to the lack of range-rate information. As the track lengthens, the Keplerian fitting of measurements shows its fundamental flaw, with added information deteriorating the estimation due to the pairing of non–homogeneous data (disk-shaped covariance), with an unsuitable dynamical model.

Table 6
Constants used for the analytical J_2 propagator developed in Section 3.3.2.

μ (km^3/s^2)	R_e (km)	J_2
398600.4418	6378.137	$1.082626683553 \cdot 10^{-3}$

GTDS suffers less from the Kepler approximation thanks to the lack of weighting, enabling error averaging. The approximated J_2 method performs best overall, particularly for the longest radar tracks.

Fig. 7 shows the uncertainty evolution for different track lengths. GTDS is more conservative in uncertainty estimation, partly due to the absence of range-rate data and the indirect use of measurement uncertainty. The information in Fig. 7 does not consider correlations, providing an incomplete picture of the covariance. The evolution is compatible with the errors, suggesting correct behavior of this estimation method. The Keplerian fit of radar observables suffers from overconfidence for tracks longer than 100 s,

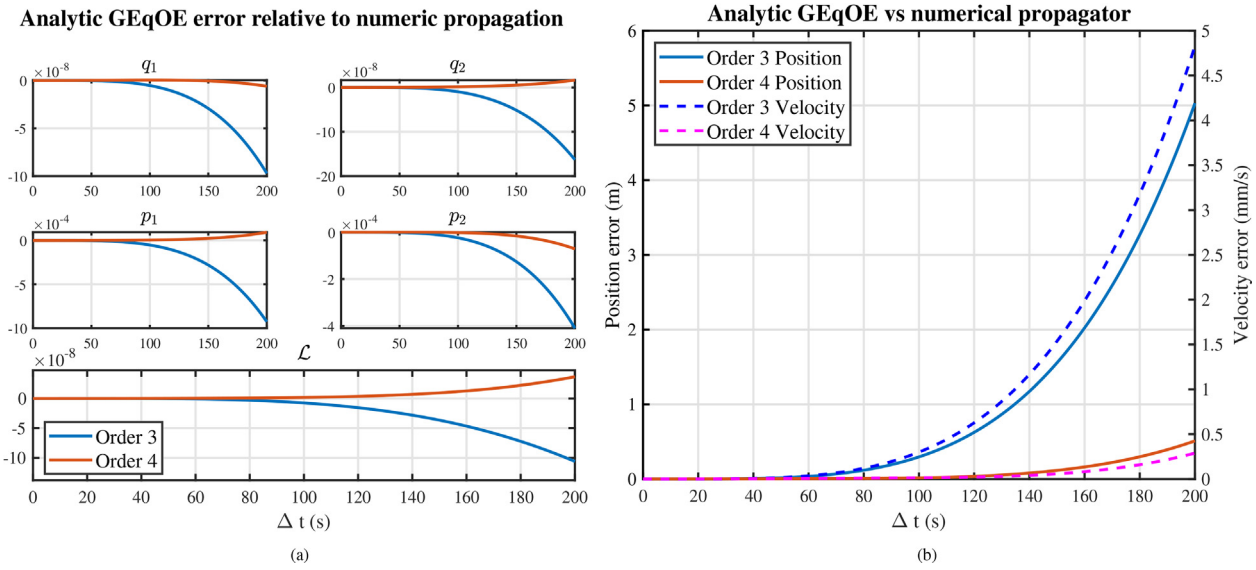

Fig. 4. GEqOE Taylor expansion relative error improves by an order of magnitude with each added term for the first 200 s. The normalizing value (for relative error computation) is the numerical propagation output with 10^{-14} tolerance (4a). Cartesian error is computed with the fourth-order approximation (4b).

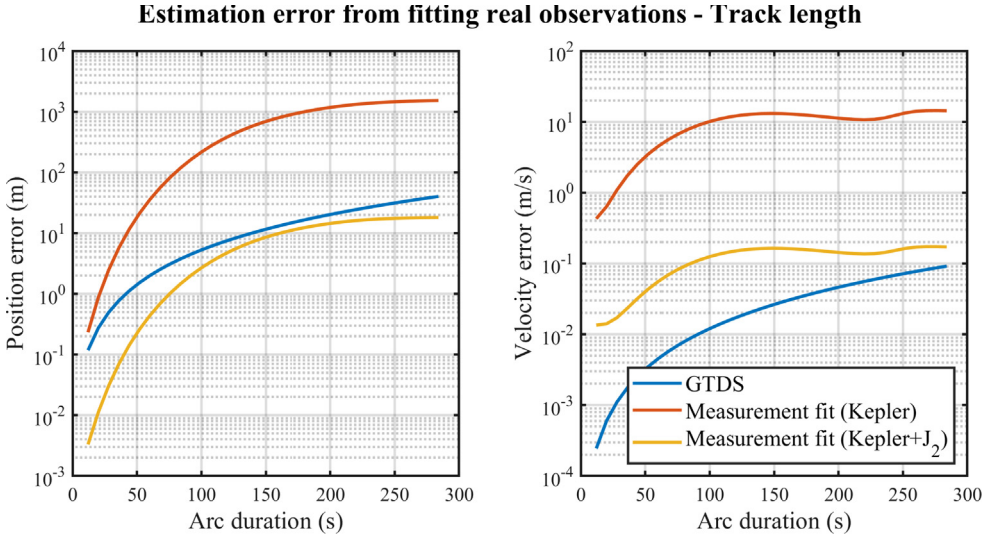

Fig. 5. Fitting errors (at t_0) for decreasing radar track durations using the three main IOD algorithms from Section 3. The same radar track as in Figs. 2 and 3 is used. All fittings use true measurement values.

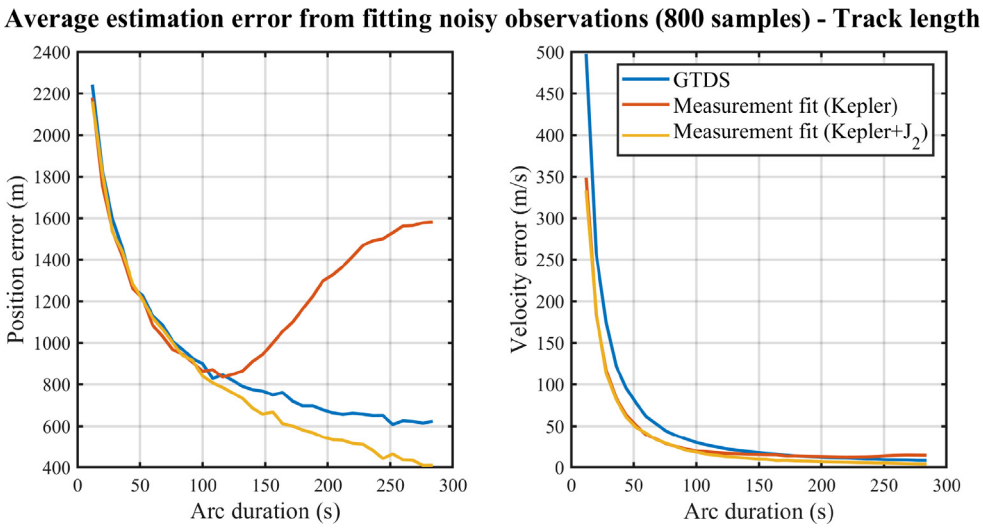

Fig. 6. Fitting errors for decreasing radar track durations using the three main IOD algorithms from Section 3, with added noise and averaged over multiple samples. All fittings use noisy measurements.

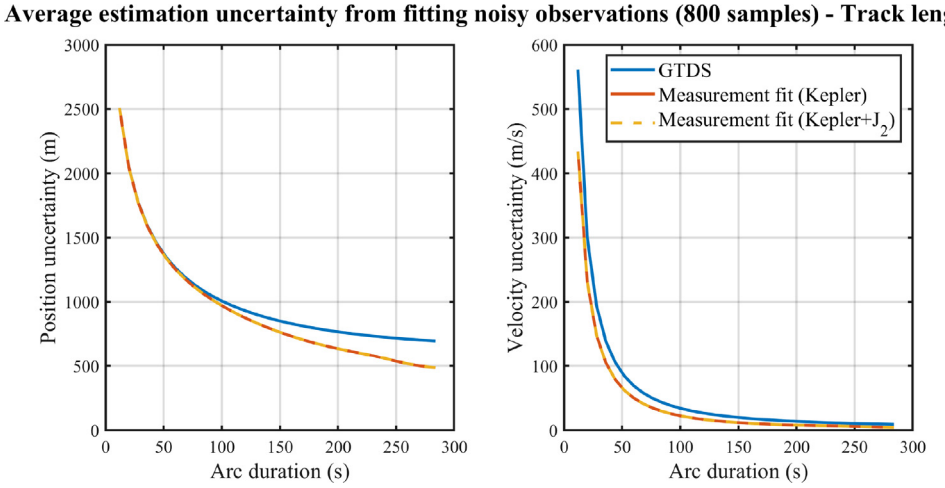

Fig. 7. Estimation uncertainty using the three main IOD methods from Section 3, with added noise and averaged over multiple samples. Uncertainty displayed: square root of the sum of eigenvalues for position and velocity blocks of the uncertainty matrix C_y, a conservative representation not considering correlations.

with uncertainty decreasing as more measurements are added, but the error not evolving accordingly. A more comprehensive exploration of uncertainty realism is conducted in Section 4.5.1 using a broader dataset.

4.3. Preliminary testing of OPOD

The IOD method that includes information of inclination (i) and right ascension of the ascending node (Ω), see Section 3.4, is tested here. First a check is performed on the degree of predictability of the orbital plane and the expected uncertainty for two different LEO. The presence of maneuvers is also considered. The fitting method is then assessed with varying virtual measurement uncertainties on the same test track as in Section 4.2 and different track lengths.

4.3.1. Orbital plane predictability check

Orbital plane predictability is first tested with a circular LEO ($a = 8600$ km, $i = 60°$). Fig. 8a compares high-fidelity dynamics versus a simple propagation, showing prediction errors for i and Ω. The high-fidelity model uses True dynamics (Table 1) with the Sentinel-1A HF model, while the simple model uses LF dynamics without atmospheric effects, including only luni-solar perturbation and degree/order 4 harmonics. A Monte-Carlo approach samples position ($\sigma_r \approx 30$ m) and velocity ($\sigma_v \approx 0.2$ m/s). Results indicate high predictability with angular errors for i and Ω around 10^{-4} degrees, σ values up to 10^{-3}, contrasting with position errors up to 13 km after 5 days. The second example (Fig. 8b), with $a = 6900$ km and $e = 10^{-4}$, requires higher fidelity (degree/order 20 harmonics) and

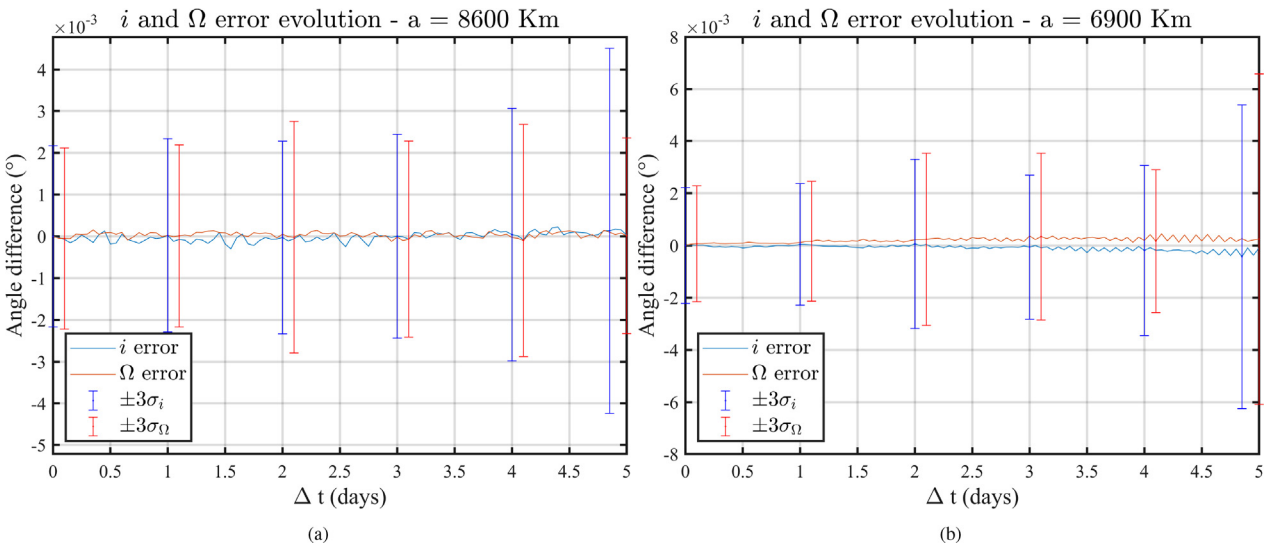

Fig. 8. Prediction error for inclination and RAAN is low using only degree/order 4 Earth harmonics and luni-solar perturbation for $a = 8600$ km (8a). For $a = 6900$ km, higher fidelity with degree/order 20 harmonics and a simple Harris-Priester atmosphere model is needed, resulting in good orbital plane predictions after 5 days (8b).

includes atmospheric effects (Modified Harris-Priester model in Orekit, Hatten and Russell (2017)). Errors for the orbital plane remain similar, but position error increases to 33 km.

These findings indicate that even a low-fidelity propagator can accurately predict the orbital plane in the absence of maneuvers. The next step is to assess the effects of maneuvers on this prediction. This was tested for a series of maneuvered cases with variations in maneuver instant and direction (5 directions, 2 instants after t_0). An impulsive value of 0.2 m/s, considered high from previous works (Montilla et al., 2023b), was used. Error evolution for all cases is shown in Fig. 9. Notable changes in inclination and RAAN occur for out-of-plane maneuvers, while prograde and retrograde maneuvers significantly affect Ω due to changes in the semi-major axis, affecting the J_2 secular rate. These examples illustrate expected errors in orbital plane prediction despite maneuvers.

The proposed method uses predicted i and Ω at the estimation epoch as extra measurements. Considering possible maneuver effects, it is crucial to use reasonable uncertainties for these virtual measurements. Overconfident values would impose constraints incompatible with measurements of a maneuvered spacecraft, inducing estimation errors. These uncertainties should be around $5 \cdot 10^{-3}$ degrees; their validity and impact on estimation are discussed next.

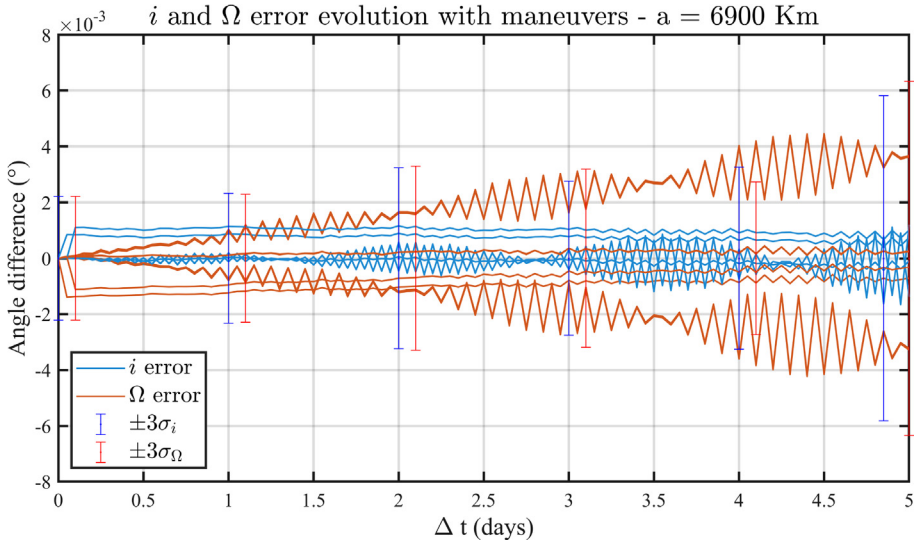

Fig. 9. For 10 maneuvered cases, predicted errors of i and Ω can exceed those in the non-maneuvered case (Fig. 8b), but remain around $5 \cdot 10^{-3}$ degrees after 5 days.

4.3.2. Effect of the i and Ω virtual measurements on the estimation error

This section tests the OPOD method and the effect of orbital plane uncertainty on estimation error. Using initial conditions S1A-1 (Table 4), the Sentinel-1A HF model is simulated with 4 maneuvered cases. A long track from Radar 3, occurring 3.6 days after t_0, is sampled and used to derive average results for varying track durations. The predicted orbital plane is calculated using the LF model. Identical i and Ω values are used for all tests with the J_2 fitting method.

Fig. 10 summarizes expected improvements for different uncertainty magnitudes. The orbit here is higher than in Fig. 9, and the prediction model has higher fidelity (Table 1), resulting in lower prediction errors (about 10% weaker J_2 effect).

The non-maneuvered case serves as a reference, showing that precise predicted i and Ω always improve the estimation. However, with large uncertainties (e.g., $5 \cdot 10^{-2}$ degrees), the improvement is reduced. Compared to Fig. 6 (Left), there is a slight reduction in estimation error, especially for shorter tracks. Reducing uncertainty by an order of magnitude significantly lowers error, particularly for very short tracks (1 km decrease in position error). Further reduction mainly affects longer tracks, with diminishing improvements when uncertainty becomes unreasonably low.

Maneuvers affect estimation accuracy, sometimes negatively. For *Out-of-plane* maneuvers, overconfidence in extra information increases prediction error for longer tracks. The estimation uncertainty always decreases with reduced $\sigma_{i,\Omega}$, leading to an overconfident estimation. This shows that uncertainties smaller than $\sigma_{i,\Omega} = 5 \cdot 10^{-3}$ degrees are not recommended for the maneuvers considered here. The *Prograde* maneuver also shows a slight error increase when orbital plane information is assumed too precise, primarily affecting Ω due to J_2 perturbation. The *Radial-out* case shows negligible error increase.

For maneuvers up to 0.2 m/s, assuming a standard deviation of $\sigma_{i,\Omega} = 5 \cdot 10^{-3}$ degrees for predicted orbital plane error is safe for state estimation. The impact on estimation statistics for this augmented method is discussed in Section 4.5.2.

4.4. Simulated scenarios

The goal of this testing is to establish realistic expectations for the estimation algorithms with varying track lengths and data density. In each scenario, the satellite's true state at t_0 sets the true orbit, which remains invariant. Testing the OPOD method requires computing the predicted orbital plane. To introduce variability in prediction accuracy, scenarios include a non-maneuvered case and various combinations of impulse value (N_{imp}), maneuver direction (N_{dir}), and maneuver instant after t_0 (N_t). Each of these $N_{imp}N_{dir}N_t + 1$ cases generates a battery of tracks (N_{int}) in a radar station within a given integration window. All tracks are individually sampled N_{ms} times to generate estimation statistics. The Mahalanobis Distance squared of the estimation error (k^2) is computed and compared to the theoretical distribution.

If the fitting methodology does not require information outside radar observables, the scenario variability only generates more (slightly) different tracks. Scenarios STARL-1 and STARL-2, which do not consider maneuvers, increase track length variety for testing the 3 main IOD algorithms. Thus, these scenarios do not require LF satellite model or initial state uncertainty information. The uncertainty aspect is relevant when including predicted

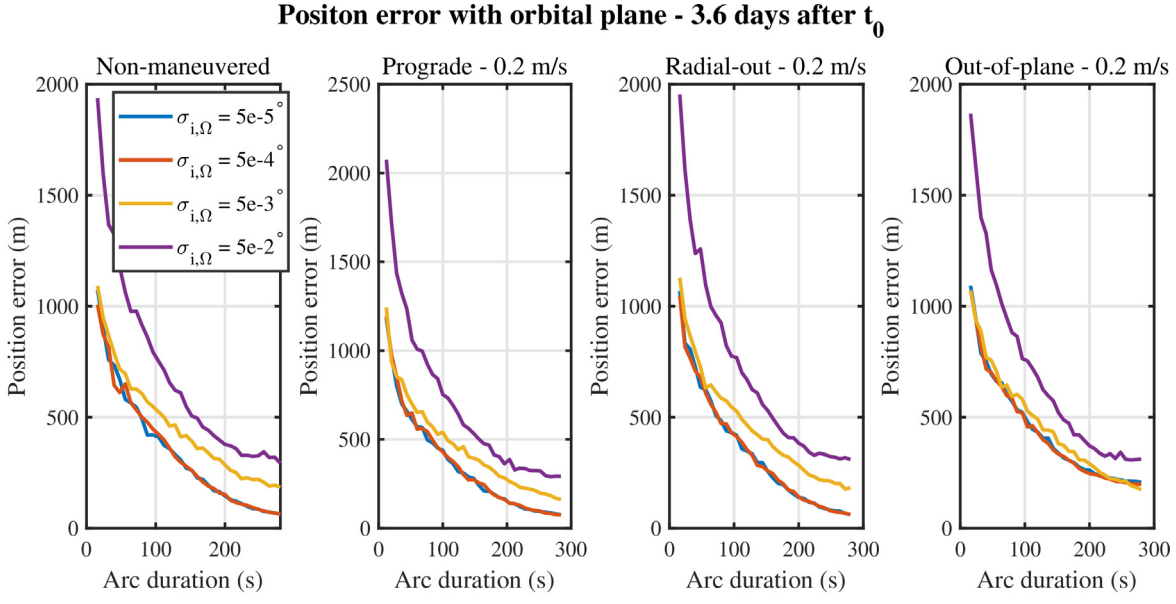

Fig. 10. Average error with orbital plane information added using the J_2 analytical estimation method for a radar track 3.6 days after t_0, with 500 measurement samples. Different maneuvered cases are compared, focusing on the uncertainty in i and Ω.

i and Ω, derived from a sampled initial state around the true one. A total of N_{sp} initial samples are propagated individually, with one randomly chosen for the estimation computation.

Five different scenarios are used to generate statistics on the methods under study. Table 8 details these scenarios. The two maneuver instants considered are 0.1 and 0.5 days after t_0. The *Low* uncertainty is locally defined with values of $5, 30.4$, and 5 meters in position, and $0.002, 0.01$, and 0.006 m/s in velocity (diagonal covariance in the LVLH frame). The integration window (with N_{int} variations) goes up to a maximum of 4 days (10 for STARL-1 and 2), depending on initial conditions and the radar station. During the maximum window, N_{int} different radar tracks are considered independently, with no combination to increase available information. The 5 impulse values used are $20, 10, 8, 5, 2$ (cm/s). The impulse directions, in Table 7, are locally defined, so $+x$ is the direction of the position vector and $+z$ is the direction of the orbit angular momentum. From 1 to 6 these are (approximately) prograde, retrograde, radial-in, radial-out, in-plane (45° from $-x$ and $+y$ in LVLH) and out-of-plane (at $+z$).

4.5. k^2 metric statistics

This section provides an in-depth analysis of the performance of the estimation methods. A series of tests evaluate the accuracy and uncertainty realism of the methods for different radar tracks from the established scenarios. Initially, a single radar pass was studied (Sections 4.2 and 4.3) without considering correlation information. The current approach uses all radar tracks from Table 8.

Following the methodology in Reihs et al. (2021), the k^2 metric (independent of predictions) is used to assess estimation uncertainty realism. This metric is $k^2 = \boldsymbol{d}^T \mathrm{C}_y \boldsymbol{d}$, with $\boldsymbol{d}$ being the vector of the difference between the fitted state and the ground truth.

For an adequate fitting model and near-linear relation between the estimated state and measurements (close to the estimated state), the k^2 statistics for a set of samples from a given track should follow a chi-square distribution with p degrees of freedom. Consequently, the mean of k^2 should be $\mu = p$, the variance $\sigma^2 = 2p$, and 10% of the samples should exceed $\chi^2_{inv}(0.9, p)$, the chi-square inverse cumulative distribution function of p degrees of freedom at the 90th percentile.

4.5.1. k^2 statistics on the IOD methods

For Radar 1 simulations in Table 8, Figs. 11–13 show k^2 statistics for full state, position, and velocity estimations. The horizontal black line indicates the expected value. Radar 1 and 2 results are treated separately due to measurement rates affecting fitting behavior.

KEP and KEP+J_2 fittings perform poorly for very short tracks (<21 s or 4 measurements), at least in regards to the uncertainty realism of the estimations. Fig. 14 shows velocity errors for a short track fitted with GTDS and KEP+J2. The distribution of the proposed method differs from the analytical covariance due to the linear approximation in the least-squares algorithm being inaccurate. As the radar tracks get shorter the uncertainty region increases, and the linear approximation ceases to be sufficiently good. In other words, the linear approximation of the covariance given by the linear least-squares method is only good when the uncertainty is localized close to the estimate, and degrades when this region becomes too large. Position estimation on the other hand has a slight bias in the smaller variance direction (not shown here), penalizing k^2. This leads to abnormally high $\chi^2_{inv}(0.9, p)$ outliers, indicating potential reliability issues for maneuver detection metrics on short tracks. GTDS behaves as expected for short tracks.

For more than 5 measurements, KEP and KEP+J_2 improve as non-linearity and position bias decrease. KEP +J_2 full state estimation behaves as indicated by the analytical covariance, even for longer Starlink-2 tracks. KEP velocity estimation degrades due to bias from 50 s and upwards, but position is unaffected.

Despite no visible degradation in position and velocity separately, GTDS has increased full state k^2 values for

Table 7
The six impulse directions used in all scenarios are defined in the LVLH frame (or QSW in OREKIT).

Direction	d_x	d_y	d_z
1	0	0.9397	0.3420
2	0	−0.9397	0.3420
3	−0.9397	0	0.3420
4	0.9397	0	0.3420
5	−0.7071	0.7071	0
6	0	0	1

Table 8
Scenarios used for the simulated data generation and metric testing. All of them use the same 6 different maneuver directions, in Table 7. I.C stands for initial conditions.

SC Name	HF Satellite	LF Satellite	Radar Station	I.C.	I.Uncertainty	N_{sp}	N_{imp}	N_{dir}	N_t	N_{int}	N_{ms}
SEN-1A-1	Sentinel-1A	Sentinel-$1A_1$	Radar 1	S1A-1	Low	50	5	6	2	4	600
SEN-1A-2	Sentinel-1A	Sentinel-$1A_1$	Radar 2	S1A-1	Low	35	5	6	2	15	600
SW-C-1	Swarm-C	Swarm-C_1	Radar 1	SWC-1	Low	50	5	6	2	4	600
STARL-1	Starlink-1	-	Radar 1	SRL-1	-	-	0	-	-	13	600
STARL-2	Starlink-2	-	Radar 1	SRL-2	-	-	0	-	-	16	600

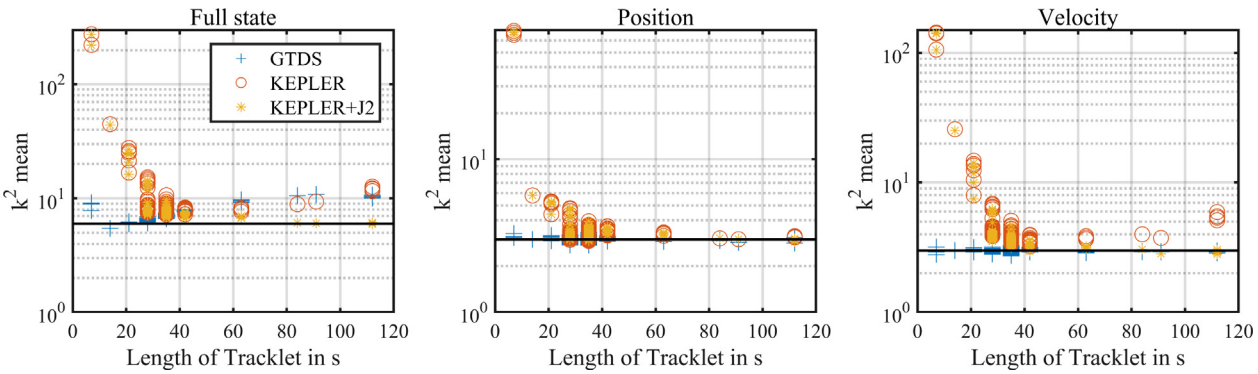

Fig. 11. Estimation only k^2 mean values for Radar 1 ($r_t = 7$ seconds). Each radar track in the scenarios SEN-1A-1, SW-C-1, STARL-1 and STARL-2 is sampled 600 times and the k^2 statistics of the corresponding method are computed.

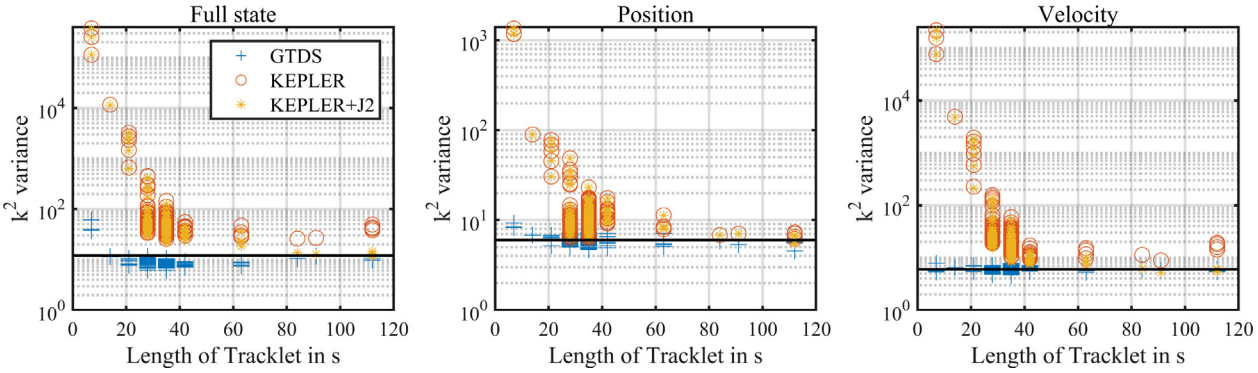

Fig. 12. Estimation only k^2 variance values for Radar 1 ($r_t = 7$ seconds). Each radar track in the scenarios SEN-1A-1, SW-C-1, STARL-1 and STARL-2 is sampled 600 times and the k^2 statistics of the corresponding method are computed.

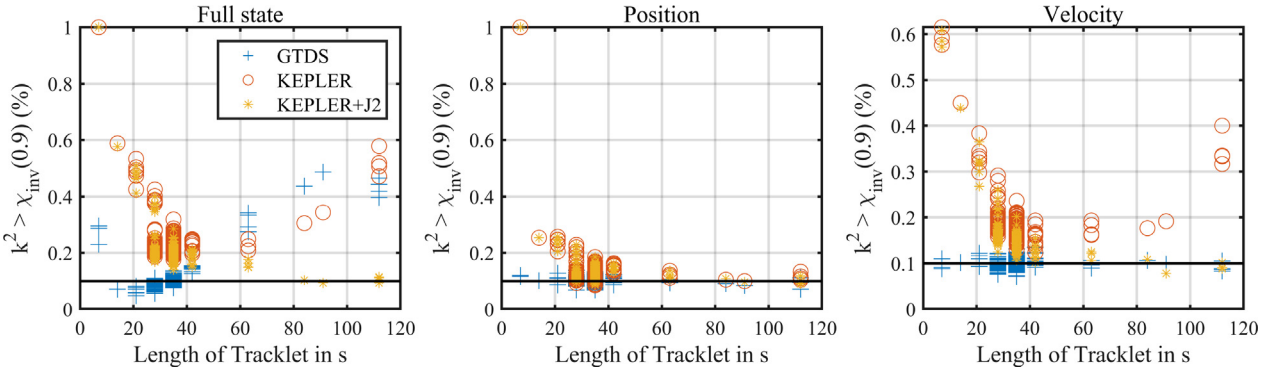

Fig. 13. Estimation only k^2 percentage of anomalous estimations for Radar 1 ($r_t = 7$ seconds). Each radar track in the scenarios SEN-1A-1, SW-C-1, STARL-1 and STARL-2 is sampled 600 times and the k^2 statistics of the corresponding method are computed.

longer tracks, see Fig. 13, likely due to unrealistic covariance correlations, making full state estimation not recommendable for longer than 50 s tracks.

For these 7s measurement rate scenarios, short track state estimation is more reliable with GTDS, but longer tracks benefit from observable fitting with range-rate using the method in Section 3.3, as KEP+J_2 velocity errors are lower than GTDS (Fig. 14). Modifying the covariance to account for non-linearity in short tracks or inflating the position covariance in the bias direction could improve the reliability of the proposed method, but this is not considered here.

Radar 2 results (4s measurement rate) are slightly different (Figs. 15–17). The SEN-1A-2 scenario includes longer tracks, showing an extended range of metric performance. KEP degrades sooner in velocity and deviates from the ideal distribution in position for >120 s tracks (similar to Fig. 6 for Radar 3). These issues make KEP almost

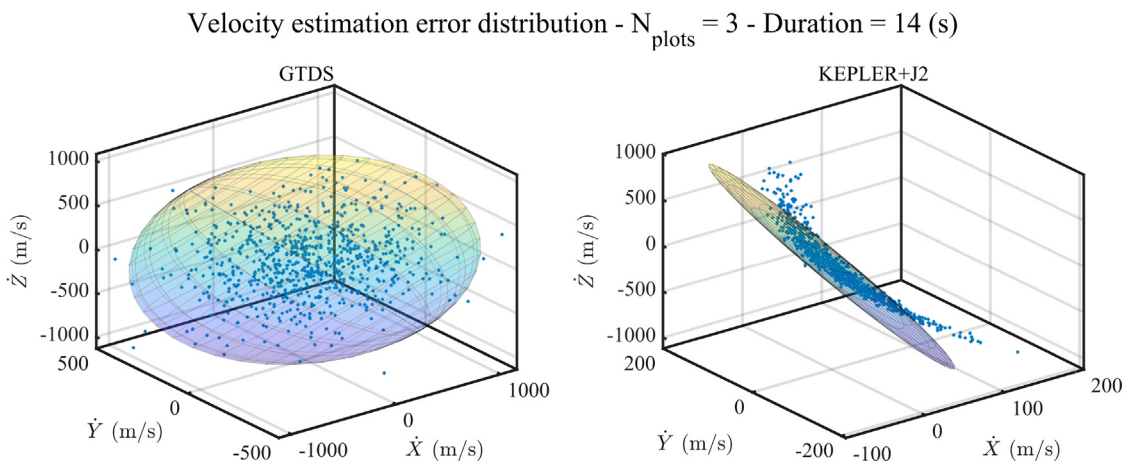

Fig. 14. Velocity error distribution for very short tracks (2–4 measurements in Radar 1) fitted with GTDS and KEP+J_2. The real distribution differs from the analytical least-squares covariance in the KEP+J_2 case, making the estimated covariance unrealistic for such short tracks.

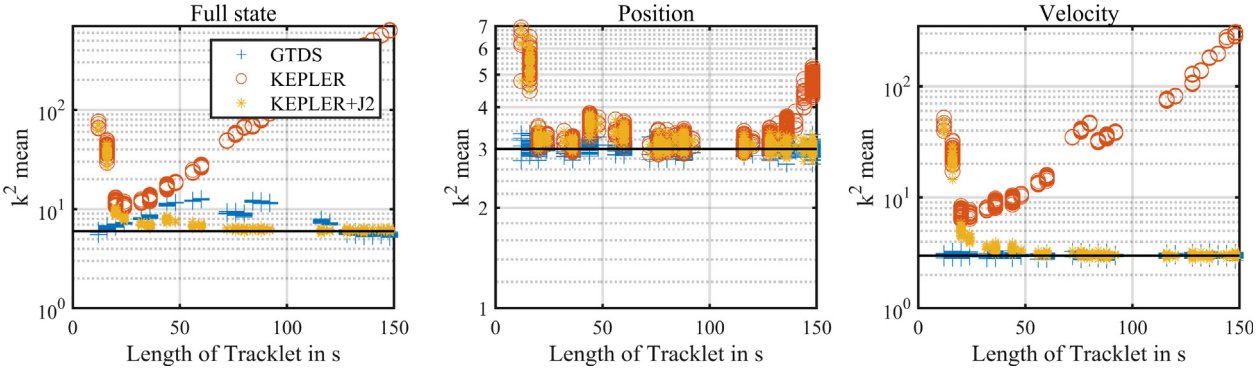

Fig. 15. Estimation only k^2 mean values for Radar 2 ($r_t = 4$ seconds).

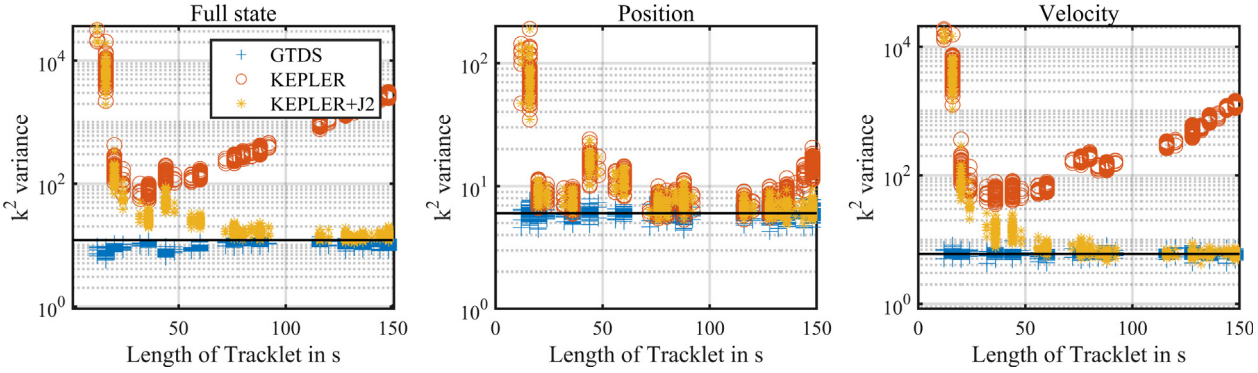

Fig. 16. Estimation only k^2 variance values for Radar 2 ($r_t = 4$ seconds).

unusable for the whole track length range when considering the full state metric (Fig. 17). GTDS shows similar behavior, with metric degradation exacerbated for around 90 s tracks but recovering for >120 s tracks, indicating compatible position-velocity correlations with the error distribution for very long tracks. However, generalizing this behavior for long single track estimation using GTDS is not recommended, as a separate test with Radar 3 showed it might not always provide adequate full state covariance correlations for very long radar tracks.

Notably, KEP+J_2 performs excellently throughout almost the complete range, only failing for very short tracks (Fig. 17). This method is not only a good estimator in terms of covariance representation realism but also offers increased accuracy due to the use of measurement uncertainty in the fitting and the inclusion of range-rate.

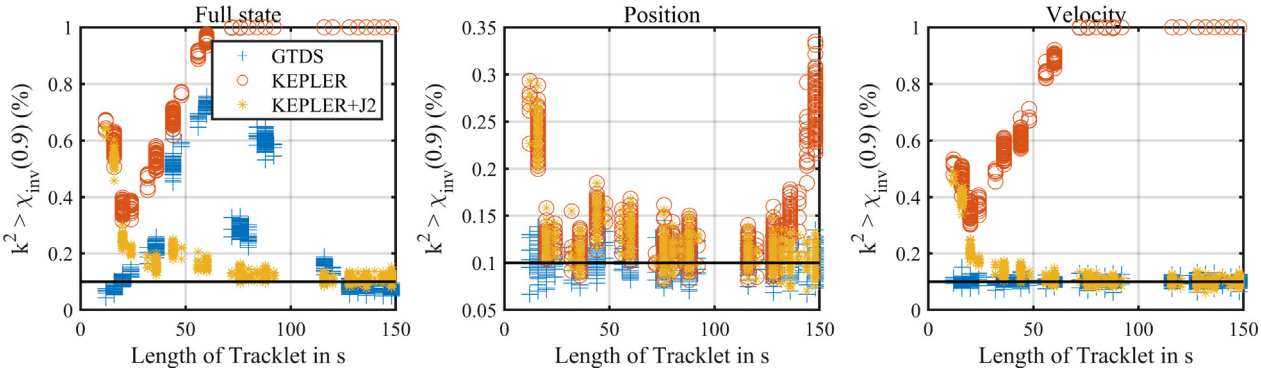

Fig. 17. Estimation only k^2 percentage of anomalous estimations for Radar 2 ($r_t = 4$ seconds).

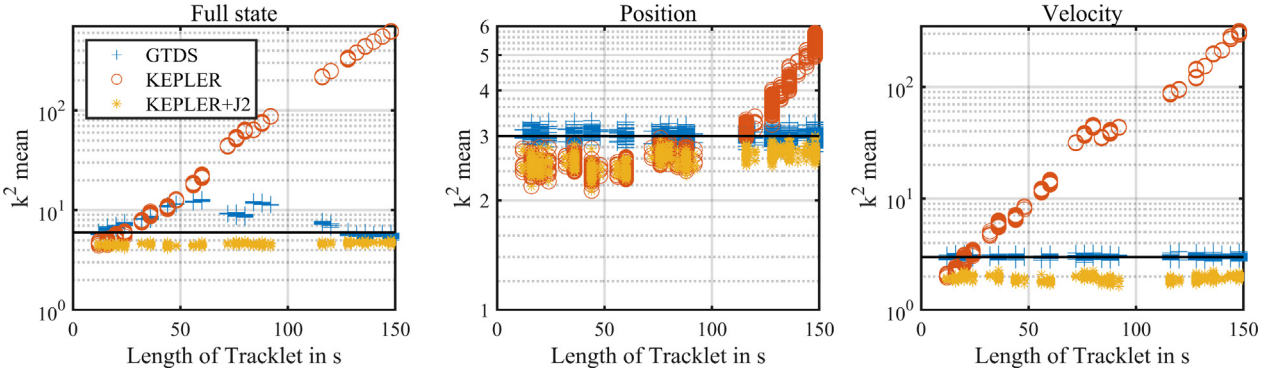

Fig. 18. Estimation only k^2 mean values for Radar 2 ($r_t = 4$ seconds), including the information of the orbital plane with $\sigma_{i,\Omega} = 5e-3^\circ$ in the KEP and KEP+J_2 methods.

4.5.2. k^2 statistics on OPOD

The SEN-1A-2 scenario has been used to test the estimation algorithms'performance, now including predicted orbital plane information. For each sampled radar track, the propagated initial condition information (randomly chosen from the I.C. sampling) was used to include predicted inclination and RAAN in the fitting. This was only done with the radar observables fitting methods, as GTDS is unweighted and does not allow for non-position measurements.

Fig. 18 shows that including orbital plane information has little effect on KEP fittings, only solving the issue with very short tracks but not addressing the degradation for longer ones. However, KEP+J2 sees its only drawback fixed and now behaves more appropriately for all track lengths. Although the obtained k^2 values are lower than expected (Fig. 20), a conservative covariance is generally more desirable to avoid false correlations. This is due to the virtual measurements being more consistent than indicated by the used uncertainty value ($\sigma_{i,\Omega} = 5e-3^\circ$ in all

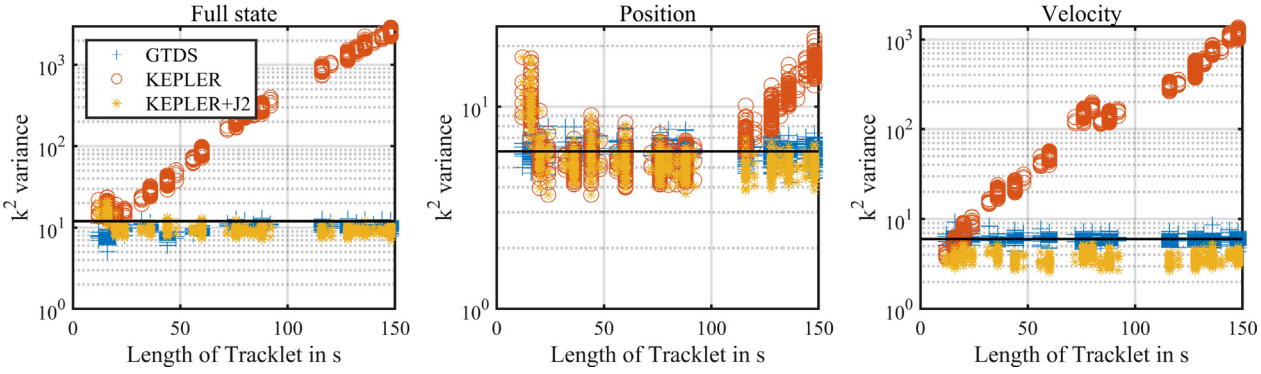

Fig. 19. Estimation only k^2 variance values for Radar 2 ($r_t = 4$ seconds), including the information of the orbital plane with $\sigma_{i,\Omega} = 5e-3^\circ$ in the KEP and KEP+J_2 methods.

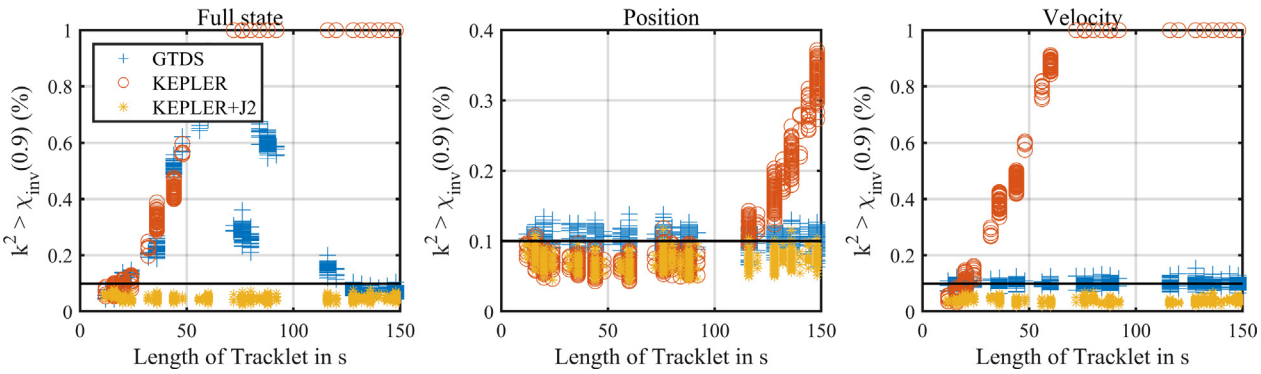

Fig. 20. Estimation only k^2 percentage of anomalous estimations for Radar 2 ($r_t = 4$ seconds), including the information of the orbital plane with $\sigma_{i,\Omega} = 5e-3^\circ$ in the KEP and KEP+J_2 methods.

cases), suggesting there is room for reducing the estimation uncertainty. GTDS results are unchanged as no extra information is added to the fit. (see Fig. 19)

Another considerably improved aspect not present in the k^2 statistics is the improved accuracy of the estimations compared to the GTDS method. This is not surprising, as the augmented methodology uses range-rate and orbital plane data to generate a better estimation in all aspects, including uncertainty realism.

5. Conclusions

This work introduces a novel approach to initial orbit determination using data from a single radar track combined with the predicted orbital plane of the object. Focusing on the need for rapid algorithms in operational scenarios, a least-squares fitting procedure incorporating an analytically formulated approximation of the dynamics under the J_2 perturbation is developed. The algorithm includes range-rate observables, distinguishing it from similar methods. A comprehensive evaluation is conducted through simulated tests, comparing its performance against a classical range and angles fitting method (GTDS), exploring the impact of track length and measurement density on full state estimation.

Proper full state estimation using radar observables directly does not work as intended with Keplerian dynamics due to the magnitude of propagation errors being greater than precise range measurements modeled after modern radar technology. Improving the fidelity of the fitting dynamics by including the J_2 perturbation solves this issue while maintaining the fully analytical aspect of the methodology. The resulting fast IOD method is applicable to maneuver detection and finding correlations between cataloged objects and tracks.

The proposed method behaves as expected for tracks longer than 40 s, especially with high data density. However, there is a problem for shorter arcs, where the nonlinear relation between the estimate and radar observables affects the velocity part of the estimation. Covariance inflation post-processing could be applied to take advantage of the higher quality estimation.

The developed method admits the inclusion of chosen parts of the predicted state as virtual measurements. Given the orbital plane's stability in LEO and relatively short integration windows, the precision of predicted i and Ω justifies their inclusion in the estimation process. The resulting method, denoted as OPOD, shows improved accuracy and reliability for all track lengths.

The analytical time derivatives of the GEqOE equations of motion developed in this work could be employed in an enhanced numerical propagator that makes use of higher order derivatives, potentially improving accuracy and reducing the total number of steps needed for a given propagation length and tolerance. This line of research is currently being pursued as an extended application of the work presented here. Another promising avenue for future research is the direct fitting of GEqOEs. This approach would allow for the incorporation of range-rate information into the estimation process and could potentially improve uncertainty representation for the linear approximation of the covariance in the context of very short tracks. By leveraging the inherent structure of GEqOEs, where two elements are functions of inclination and longitude of the node, this method could naturally integrate orbital plane orientation information, as demonstrated in our OPOD method.

Declaration of Competing Interest

The authors declare that they have no known competing financial interests or personal relationships that could have appeared to influence the work reported in this paper.

Acknowledgments

Jose M. Montilla and R. Vazquez gratefully acknowledge support by grant TED2021-132099B-C33 funded by MICIU/AEI/10.13039/501100011033 and by "European Union NextGenerationEU/PRTR". Special thanks are due to Guillermo Escribano for his help in developing the ideas and methods in this work.

During the preparation of this work the author(s) used ChatGPT in order to revise and correct grammar and

refine the language. After using this tool/service, the authors reviewed and edited the content as needed and take full responsibility for the content of the publication.

Appendix A. Auxiliary functions

A.1. Radar measurement function derivatives

The measurements provided by the radar in LEO are range (ρ), azimuth (Az), elevation (el) and range-rate ($\dot{\rho}$). The observation function $[\rho, Az, el, \dot{\rho}] = h(\boldsymbol{y}, t)$ of these observables is given by:

$$\begin{aligned}
\rho &= [(\boldsymbol{r}-\boldsymbol{P}_R)^\intercal(\boldsymbol{r}-\boldsymbol{P}_R)]^{1/2} = [\rho^\intercal\rho]^{1/2},\\
Az &= \operatorname{atan2}(\boldsymbol{e}_1^\intercal\rho\rfloor_R, \boldsymbol{e}_2^\intercal\rho\rfloor_R) = \operatorname{atan2}\left(\boldsymbol{e}_1^\intercal \mathrm{T}_I^R\rho, \boldsymbol{e}_2^\intercal \mathrm{T}_I^R\rho\right),\\
el &= \arcsin\left(\frac{\boldsymbol{e}_3^\intercal\rho\rfloor_R}{\rho}\right) = \arcsin\left(\frac{\boldsymbol{e}_3^\intercal \mathrm{T}_I^R\rho}{\rho}\right),\\
\dot{\rho} &= \tfrac{1}{\rho}(\boldsymbol{r}-\boldsymbol{P}_R)^\intercal(\boldsymbol{v}-\boldsymbol{V}_R) = \tfrac{\rho^\intercal\boldsymbol{u}}{\rho},
\end{aligned} \tag{A.1}$$

where $\rho = \boldsymbol{r} - \boldsymbol{P}_R$ and $\boldsymbol{u} = \boldsymbol{v} - \boldsymbol{V}_R$. The unit vectors $(\boldsymbol{e}_1, \boldsymbol{e}_2, \boldsymbol{e}_3)$ form a Cartesian frame base. The fitting algorithms in Sections 3.2 and 3.3 require the derivatives of these measurements with respect to position ($\boldsymbol{r}$) and velocity ($\boldsymbol{v}$):

$$\frac{\partial h}{\partial \boldsymbol{y}} = \begin{bmatrix} \rho_{\boldsymbol{r}} & \rho_{\boldsymbol{v}} \\ Az_{\boldsymbol{r}} & Az_{\boldsymbol{v}} \\ el_{\boldsymbol{r}} & el_{\boldsymbol{v}} \\ \dot{\rho}_{\boldsymbol{r}} & \dot{\rho}_{\boldsymbol{v}}. \end{bmatrix}. \tag{A.2}$$

The explicit functions of these derivatives are:

$$\begin{aligned}
\rho_{\boldsymbol{r}} &= \tfrac{\rho^\intercal}{\rho}, & \rho_{\boldsymbol{v}} &= \boldsymbol{0}^\intercal,\\
Az_{\boldsymbol{r}} &= \tfrac{1}{1+\tan^2(Az)}\left[\boldsymbol{e}_1^\intercal - \tan(Az)\boldsymbol{e}_2^\intercal\right]\tfrac{\mathrm{T}_I^R}{\boldsymbol{e}_2^\intercal\rho\rfloor_R}, & Az_{\boldsymbol{v}} &= \boldsymbol{0}^\intercal,\\
el_{\boldsymbol{r}} &= \tfrac{1}{\sqrt{1-\sin^2(el)}}\left[\boldsymbol{e}_3^\intercal \mathrm{T}_I^R - \sin(el)\rho_{\boldsymbol{r}}\right]\tfrac{1}{\rho}, & el_{\boldsymbol{v}} &= \boldsymbol{0}^\intercal,\\
\dot{\rho}_{\boldsymbol{r}} &= (\boldsymbol{u} - \dot{\rho}\rho_{\boldsymbol{r}})\tfrac{1}{\rho}, & \dot{\rho}_{\boldsymbol{v}} &= \tfrac{\rho}{\rho},
\end{aligned} \tag{A.3}$$

which requires the knowledge of radar's inertial position ($\boldsymbol{P}_R$), velocity ($\boldsymbol{V}_R$) and orientation (T_I^R).

A.2. Time derivatives of the inverse function

In Section 3.3, the linear least-squares algorithm is applied to a dynamical model that includes the J_2 perturbation using the GEqOE from Baù et al. (2021). To maintain the analytical aspect of the fitting method, a Taylor expansion has been developed. The coefficients of this expansion are detailed in A.4, which extensively uses the inverse function $\not{f}_s = \frac{1}{s}$ and its time derivatives:

$$\begin{aligned}
\dot{\not{f}}_s &= -\tfrac{\dot{s}}{s^2},\\
\ddot{\not{f}}_s &= 2\tfrac{\dot{s}^2}{s^3} - \tfrac{\ddot{s}}{s^2},\\
\dddot{\not{f}}_s &= 6\tfrac{\dot{s}\ddot{s}}{s^3} - \tfrac{\dddot{s}}{s^2} - 6\tfrac{\dot{s}^3}{s^4},\\
\overset{(4)}{\not{f}}_s &= 8\tfrac{\overset{(3)}{s}\dot{s}}{s^3} + 6\tfrac{\ddot{s}^2}{s^3} - 36\tfrac{\dot{s}^2\ddot{s}}{s^4} - \tfrac{\overset{(4)}{s}}{s^2} - 24\tfrac{\dot{s}^4}{s^5}.
\end{aligned} \tag{A.4}$$

A.3. Time derivatives of the function of s times $\dot{s}$

As with the inverse function in A.2, the function that multiplies s by its time derivative $\dot{s}$, $\not{g}_s = s\dot{s}$, is repeatedly used in the derivation of the J_2 Taylor propagator (see A.4). The time derivatives of $\not{g}_s$ are included here:

$$\begin{aligned}
\dot{\not{g}}_s &= \dot{s}^2 + s\ddot{s},\\
\ddot{\not{g}}_s &= 3\dot{s}\ddot{s} + s\dddot{s}\\
\dddot{\not{g}}_s &= 3\ddot{s}^2 + 4\dot{s}\overset{(3)}{s} + s\overset{(4)}{s},\\
\overset{(4)}{\not{g}}_s &= 10\ddot{s}\overset{(3)}{s} + 5\dot{s}\overset{(4)}{s} + s\overset{(5)}{s}.
\end{aligned} \tag{A.5}$$

A.4. Time derivatives of the J_2 GEqOE equations of motion

To develop an efficient J_2 perturbation propagator, this work uses a Taylor expansion of the solution in terms of GEqOE (Baù et al., 2021). First, the equations of motion are simplified into a compact form (Eq. A.6), utilizing the inverse function (see A.2). This section includes the time derivatives of Eq. A.6 up to fourth order. All simplifications are defined in A.4.2, facilitating a systematic application of the chain rule. From A.4.1–A.4.4, all steps for computing the Taylor J_2 propagator coefficients are included.

A.4.1. First order derivatives

The first order time derivatives of the GEqOE can be computed with:

$$\begin{aligned}
\dot{\nu} &= 0, & \dot{p}_1 &= p_2(\mathscr{A} - w_h) - \not{f}_c\xi_1\mathcal{U}, & \dot{p}_2 &= p_1(w_h - \mathscr{A}) + \not{f}_c\xi_2\mathcal{U},\\
\dot{q}_1 &= -I\mathscr{s}_L, & \dot{q}_2 &= -I\mathscr{c}_L, & \dot{\mathcal{L}} &= \nu + \mathscr{A} - w_h - \not{f}_c\Gamma\mathcal{U},
\end{aligned} \tag{A.6}$$

where $\mathscr{s}_L = \sin L$, $\mathscr{c}_L = \cos L$. The rest of definitions for the elements in Eq. (A.6) can be found next. Higher order derivatives will require the computation of:

$$\begin{aligned}
\cos L &= \tfrac{X}{r},\\
\sin L &= \tfrac{Y}{r},\\
\dot{X} &= \dot{r}\cos L - \tfrac{h}{r}\sin L,\\
\dot{Y} &= \dot{r}\sin L + \tfrac{h}{r}\cos L.
\end{aligned} \tag{A.7}$$

A.4.2. Second order derivatives

The second order time derivatives of the GEqOE can be computed with:

$$\begin{aligned}
\ddot{v} &= 0, & \ddot{q}_1 &= -\ddot{I}\vartheta_L - I\ddot{\vartheta}_L,\\
\ddot{p}_1 &= \ddot{p}_2(\mathscr{a} - w_h) + p_2(\ddot{\mathscr{a}} - \ddot{w}_h) - \left(\ddot{\mathscr{f}}_c\xi_1 + \mathscr{f}_c\ddot{\xi}_1\right)\mathcal{U} - \mathscr{f}_c\xi_1\dot{\mathcal{U}}, & \ddot{q}_2 &= -\ddot{I}c_L - I\ddot{c}_L,\\
\ddot{p}_2 &= \ddot{p}_1(w_h - \mathscr{a}) + p_1(\ddot{w}_h - \ddot{\mathscr{a}}) + \left(\ddot{\mathscr{f}}_c\xi_2 + \mathscr{f}_c\ddot{\xi}_2\right)\mathcal{U} + \mathscr{f}_c\xi_1\dot{\mathcal{U}}, & \ddot{\mathcal{L}} &= \ddot{\mathscr{a}} - \ddot{w}_h - (\ddot{\mathscr{f}}_c\Gamma + \mathscr{f}_c\dot{\Gamma})\mathcal{U} - \mathscr{f}_c\Gamma\dot{\mathcal{U}}.
\end{aligned} \tag{A.8}$$

All the elements that appear in Eq. (A.8) are computed with the following formulation. The first time derivative of $\hat{z}$ is computed from:

$$\begin{aligned}
\hat{z} &= \tfrac{2(Yq_2 - Xq_1)}{r(1+q_1^2+q_2^2)} = \tfrac{\mathcal{C}}{\mathcal{D}} = \mathcal{C}\mathscr{f}_{\mathcal{D}}, & \dot{\hat{z}} &= \dot{\mathcal{C}}\mathscr{f}_{\mathcal{D}} + \mathcal{C}\dot{\mathscr{f}}_{\mathcal{D}},\\
\mathcal{C} &= 2(Yq_2 - Xq_1), & \dot{\mathcal{C}} &= 2\left(\dot{Y}q_2 + Y\dot{q}_2 - \dot{X}q_1 - X\dot{q}_1\right),\\
\mathcal{D} &= r(1+q_1^2+q_2^2) = rq_s, & \dot{\mathcal{D}} &= \dot{r}q_s + r\dot{q}_s,\\
q_s &= (1+q_1^2+q_2^2), & \dot{q}_s &= 2(q_1\dot{q}_1 + q_2\dot{q}_2),
\end{aligned} \tag{A.9}$$

where $\dot{\mathscr{f}}_{\mathcal{D}}$ is calculated from $\dot{\mathcal{D}}$. The first time derivative of $\mathcal{U}$ and U_z are:

$$\begin{aligned}
\mathcal{U} &= -\tfrac{A}{r^3}(1 - 3\hat{z}^2) = -AU_z\mathscr{f}_{r^3}, & \dot{\mathcal{U}} &= -A\left(\dot{U}_z\mathscr{f}_{r^3} + U_z\dot{\mathscr{f}}_{r^3}\right),\\
U_z &= (1 - 3\hat{z}^2), & \dot{U}_z &= -6\hat{z}\dot{\hat{z}}.
\end{aligned} \tag{A.10}$$

The value $\dot{\mathscr{f}}_{r^3}$ in Eq. (A.10) is computed from the derivative of r^3:

$$\frac{d(r^3)}{dt} = \dot{r}_c = 3r^2\dot{r}. \tag{A.11}$$

Given that the generalized semi-major axis is $a = (\mu/v^2)^{1/3}$, the derivative of Γ and β, which in turn allows to compute $\dot{\mathscr{f}}_{1+\beta}, \dot{\mathscr{f}}_{\beta}$ and $\dot{\mathscr{f}}_{\alpha}$, are given by:

$$\begin{aligned}
\Gamma &= \mathscr{f}_{\alpha} + \alpha(1 - r/a), & \dot{\Gamma} &= \dot{\mathscr{f}}_{\alpha} + \dot{\alpha}\left(1 - \tfrac{r}{a}\right) - \alpha\tfrac{\dot{r}}{a},\\
\alpha &= \tfrac{1}{1+\beta} = \mathscr{f}_{1+\beta}, & \dot{\alpha} &= \dot{\mathscr{f}}_{1+\beta},\\
\beta &= \sqrt{1 - p1^2 - p_2^2}, & \dot{\beta} &= \tfrac{-\dot{p}_s}{2\beta} = -\tfrac{1}{2}\dot{p}_s\mathscr{f}_{\beta},\\
p_s &= 1 + p_1^2 + p_2^2, & \dot{p}_s &= 2(p_1\dot{p}_1 + p_2\dot{p}_2).
\end{aligned} \tag{A.12}$$

The first time derivative of I is given in:

$$\begin{aligned}
I &= \tfrac{3A}{hr^3}\hat{z}(1 - q_1^2 - q_2^2) = 3A\tfrac{\hat{z}\delta}{\hbar} = 3A\hat{z}\delta\mathscr{f}_{\hbar}, & \dot{I} &= 3A\left[\left(\dot{\hat{z}}\delta + \hat{z}\dot{\delta}\right)\mathscr{f}_{\hbar} + \hat{z}\delta\dot{\mathscr{f}}_{\hbar}\right],\\
\delta &= 1 - q_1^2 - q_2^2, & \dot{\delta} &= -\dot{q}_s,\\
\hbar &= hr^3 = hr_c, & \dot{\hbar} &= \dot{h}r_c + h\dot{r}_c,\\
h &= \sqrt{c^2 - 2r^2\mathcal{U}}, & \dot{h} &= \left(g_c - 2g_r\mathcal{U} - r^2\dot{\mathcal{U}}\right)\mathscr{f}_h,\\
c &= \left(\tfrac{\mu^2}{v}\right)^{1/3}\sqrt{1 - p_1^2 - p_2^2} = \left(\tfrac{\mu^2}{v}\right)^{1/3}\beta, & \dot{c} &= \left(\tfrac{\mu^2}{v}\right)^{1/3}\dot{\beta}.
\end{aligned} \tag{A.13}$$

This includes the computation of $\dot{\mathscr{f}}_{\hbar}$ from $\dot{\hbar}$, and $\dot{\mathscr{f}}_h$ is computed from $\dot{h}$ for later use. The same goes for $\dot{\mathscr{f}}_c$ and g_c, calculated from $\dot{c}$. The first time derivative of $\mathscr{a}$ is:

$$\begin{aligned}
\mathscr{a} &= \tfrac{h-c}{r^2} = (h - c)\mathscr{f}_{r^2},\\
\dot{\mathscr{a}} &= \left(\dot{h} - \dot{c}\right)\mathscr{f}_{r^2} + (h - c)\dot{\mathscr{f}}_{r^2},\\
\tfrac{d(r^2)}{dt} &= \dot{r}_s = 2r\dot{r} = 2g_r,
\end{aligned} \tag{A.14}$$

where $\dot{\mathscr{f}}_{r^2}$ is computed from the derivation of r^2. Finally, the time derivatives of $w_h, \xi_1, \xi_2, \vartheta_L$ and c_L are:

$$\begin{aligned}
w_h &= I\hat{z}, & \dot{w}_h &= \dot{I}\hat{z} + I\dot{\hat{z}},\\
\xi_1 &= \tfrac{X}{a} + 2p_2, & \dot{\xi}_1 &= \tfrac{\dot{X}}{a} + 2\dot{p}_2,\\
\xi_2 &= \tfrac{Y}{a} + 2p_1, & \dot{\xi}_2 &= \tfrac{\dot{Y}}{a} + 2\dot{p}_1,\\
\vartheta_L &= \tfrac{Y}{r} = Y\mathscr{f}_r, & \dot{\vartheta}_L &= \dot{Y}\mathscr{f}_r + Y\dot{\mathscr{f}}_r,\\
c_L &= \tfrac{X}{r} = X\mathscr{f}_r, & \dot{c}_L &= \dot{X}\mathscr{f}_r + X\dot{\mathscr{f}}_r.
\end{aligned} \tag{A.15}$$

In this section the computation of every $\mathscr{f}_s$ time derivative has been explicitly written. In the following, these comments are omitted for the sake of brevity, and it will be assumed all instances can be computed with the corresponding derivatives of s (to the needed order).

A.4.3. Third order derivatives

The third order time derivatives of the GEqOE can be computed with:

$$\begin{aligned}
&\dddot{v} = 0,\\
&\dddot{q}_1 = -\dddot{I}\vartheta_L - 2\ddot{I}\dot{\vartheta}_L - I\ddot{\vartheta}_L,\\
&\dddot{q}_2 = -\dddot{I}c_L - 2\ddot{I}\dot{c}_L - I\ddot{c}_L,\\
&\dddot{p}_1 = \dddot{p}_2(\mathscr{a} - w_h) + 2\ddot{p}_2(\dot{\mathscr{a}} - \dot{w}_h) + p_2(\ddot{\mathscr{a}} - \ddot{w}_h) - \left(\dddot{\mathscr{f}}_c\xi_1 + 2\ddot{\mathscr{f}}_c\dot{\xi}_1 + \mathscr{f}_c\ddot{\xi}_1\right)\\
&\mathcal{U} - 2\left(\ddot{\mathscr{f}}_c\xi_1 + \mathscr{f}_c\dot{\xi}_1\right)\dot{\mathcal{U}} - \mathscr{f}_c\xi_1\ddot{\mathcal{U}},\\
&\dddot{p}_2 = \dddot{p}_1(w_h - \mathscr{a}) + 2\ddot{p}_1(\dot{w}_h - \dot{\mathscr{a}}) + p_1(\ddot{w}_h - \ddot{\mathscr{a}}) + \left(\dddot{\mathscr{f}}_c\xi_2 + 2\ddot{\mathscr{f}}_c\dot{\xi}_2 + \mathscr{f}_c\ddot{\xi}_2\right)\\
&\mathcal{U} + 2\left(\ddot{\mathscr{f}}_c\xi_2 + \mathscr{f}_c\dot{\xi}_2\right)\dot{\mathcal{U}} + \mathscr{f}_c\xi_2\ddot{\mathcal{U}},\\
&\ddot{\mathcal{L}} = \dddot{\mathscr{a}} - \dddot{w}_h - (\ddot{\mathscr{f}}_c\Gamma + 2\ddot{\mathscr{f}}_c\dot{\Gamma} + \mathscr{f}_c\ddot{\Gamma})\\
&\mathcal{U} - 2(\ddot{\mathscr{f}}_c\Gamma + \mathscr{f}_c\dot{\Gamma})\dot{\mathcal{U}} - \mathscr{f}_c\Gamma\ddot{\mathcal{U}}.
\end{aligned} \tag{A.16}$$

All the elements that appear in Eq. (A.16) are computed with the following formulation. The second time derivative of $\hat{z}$ comes from:

$$\begin{aligned}
\ddot{\hat{z}} &= \ddot{\mathcal{C}}\mathscr{f}_{\mathcal{D}} + 2\dot{\mathcal{C}}\dot{\mathscr{f}}_{\mathcal{D}} + \mathcal{C}\ddot{\mathscr{f}}_{\mathcal{D}}, & \ddot{\mathcal{C}} &= 2\left(\ddot{Y}q_2 + 2\dot{Y}\dot{q}_2 + Y\ddot{q}_2 - \ddot{X}q_1 - 2\dot{X}\dot{q}_1 - X\ddot{q}_1\right),\\
\ddot{\mathcal{D}} &= \ddot{r}q_s + 2\dot{r}\dot{q}_s + r\ddot{q}_s \to \ddot{\mathscr{f}}_{\mathcal{D}}, & \ddot{q}_s &= 2\left(\dot{q}_1^2 + q_1\ddot{q}_1 + \dot{q}_2^2 + q_2\ddot{q}_2\right).
\end{aligned} \tag{A.17}$$

The second order time derivatives of X and Y are computed with:

$$\begin{aligned}
\dot{X} &= \dot{r}\cos L - \tfrac{h}{r}\sin L = \dot{r}c_L - \omega\vartheta_L, & \ddot{X} &= \ddot{r}c_L + \dot{r}\dot{c}_L - \dot{\omega}\vartheta_L - \omega\dot{\vartheta}_L,\\
\dot{Y} &= \dot{r}\sin L + \tfrac{h}{r}\cos L = \dot{r}\vartheta_L + \omega c_L, & \ddot{Y} &= \ddot{r}\vartheta_L + \dot{r}\dot{\vartheta}_L + \dot{\omega}c_L + \omega\dot{c}_L,\\
\omega &= \tfrac{h}{r} = h\mathscr{f}_r, & \dot{\omega} &= \dot{h}\mathscr{f}_r + h\dot{\mathscr{f}}_r,\\
\dot{r} &= \tfrac{\mu}{c}(p_2\sin L - p_1\cos L) = \mu\mathscr{f}_c r_{pl}, & \ddot{r} &= \mu\left(\dot{\mathscr{f}}_c r_{pl} + \mathscr{f}_c\dot{r}_{pl}\right),\\
r_{pl} &= p_2\vartheta_L - p_1c_L, & \dot{r}_{pl} &= \dot{p}_2\vartheta_L + p_2\dot{\vartheta}_L - \dot{p}_1c_L - p_1\dot{c}_L.
\end{aligned} \tag{A.18}$$

The second time derivative of $\mathcal{U}$ and U_z can be computed with:

$$\ddot{\mathcal{U}} = -A\left(\ddot{U}_z\mathscr{f}_{r^3} + 2\dot{U}_z\dot{\mathscr{f}}_{r^3} + U_z\ddot{\mathscr{f}}_{r^3}\right), \quad \ddot{U}_z = -6\left(\dot{\hat{z}}^2 + \hat{z}\ddot{\hat{z}}\right), \quad \tfrac{d^2(r^3)}{dt^2} = \ddot{r}_c = 3(2r\dot{r}^2 + r^2\ddot{r}). \tag{A.19}$$

The second order derivatives of Γ and β are given by:

$$\begin{aligned}
\ddot{\Gamma} &= \ddot{\mathscr{f}}_{\alpha} + \ddot{\alpha}\left(1 - \tfrac{r}{a}\right) - 2\dot{\alpha}\tfrac{\dot{r}}{a} - \alpha\tfrac{\ddot{r}}{a}, & \ddot{\alpha} &= \ddot{\mathscr{f}}_{1+\beta},\\
\ddot{\beta} &= -\tfrac{1}{2}\left(\ddot{p}_s\mathscr{f}_{\beta} + \dot{p}_s\dot{\mathscr{f}}_{\beta}\right) \to \ddot{\mathscr{f}}_{1+\beta}, \ddot{\mathscr{f}}_{\beta}, & \ddot{p}_s &= 2\left(\dot{p}_1^2 + p_1\ddot{p}_1 + \dot{p}_2^2 + p_2\ddot{p}_2\right).
\end{aligned} \tag{A.20}$$

The second time derivative of I is completely defined in:

$$\begin{aligned}
\ddot{I} &= 3A\left[\left(\ddot{\hat{z}}\delta + 2\dot{\hat{z}}\dot{\delta} + \hat{z}\ddot{\delta}\right)\not{f}_{h} + 2\left(\dot{\hat{z}}\delta + \hat{z}\dot{\delta}\right)\dot{\not{f}}_{h} + \hat{z}\delta\ddot{\not{f}}_{h}\right],\\
\ddot{h} &= \ddot{h}r_c + 2\dot{h}\dot{r}_c + h\ddot{r}_c,\\
\ddot{h} &= \left(\ddot{g}_c - 2\ddot{g}_r\mathcal{U} - 4\dot{g}_r\dot{\mathcal{U}} - r^2\ddot{\mathcal{U}}\right)\not{f}_h + \left(\dot{g}_c - 2\dot{g}_r\mathcal{U} - r^2\dot{\mathcal{U}}\right)\dot{\not{f}}_h,\\
\ddot{c} &= \left(\frac{\mu^2}{\nu}\right)^{1/3}\ddot{\beta},\\
\ddot{\delta} &= -\ddot{q}_s.
\end{aligned} \tag{A.21}$$

The second time derivative of $\mathscr{d}$ results from:

$$\begin{aligned}
\ddot{\mathscr{d}} &= \left(\ddot{h} - \ddot{c}\right)\not{f}_{r^2} + 2\left(\dot{h} - \dot{c}\right)\dot{\not{f}}_{r^2} + (h - c)\ddot{\not{f}}_{r^2},\\
\frac{d^2(r^2)}{dt^2} &= \ddot{r}_s = 2\dot{g}_r.
\end{aligned} \tag{A.22}$$

The second order time derivatives of $w_h, \xi_1, \xi_2, \vartheta_L$ and c_L are:

$$\begin{aligned}
\ddot{w}_h &= \ddot{I}\hat{z} + 2\dot{I}\dot{\hat{z}} + I\ddot{\hat{z}},\\
\ddot{\xi}_1 &= \frac{\ddot{X}}{a} + 2\ddot{p}_2,\\
\ddot{\xi}_2 &= \frac{\ddot{Y}}{a} + 2\ddot{p}_1,\\
\ddot{\vartheta}_L &= \ddot{Y}\not{f}_r + 2\dot{Y}\dot{\not{f}}_r + Y\ddot{\not{f}}_r,\\
\ddot{c}_L &= \ddot{X}\not{f}_r + 2\dot{X}\dot{\not{f}}_r + X\ddot{\not{f}}_r.
\end{aligned} \tag{A.23}$$

A.4.4. Fourth order derivatives

The fourth order time derivatives of the GEqOE can be computed with:

$$\begin{aligned}
\overset{(4)}{\nu} &= 0,\\
\overset{(4)}{q}_1 &= -\ddot{I}\,\vartheta_L - 3\dot{I}\ddot{\vartheta}_L - 3\dot{I}\ddot{\vartheta}_L - I\,\overset{(4)}{\vartheta}_L,\\
\overset{(4)}{q}_2 &= -\ddot{I}\,c_L - 3\dot{I}\ddot{c}_L - 3\dot{I}\ddot{c}_L - I\,\overset{(4)}{c}_L,\\
\overset{(4)}{p}_1 &= \ddot{p}_2\left(\mathscr{d} - w_h\right) + 3\dot{p}_2\left(\dot{\mathscr{d}} - \dot{w}_h\right) + 3\dot{p}_2\left(\ddot{\mathscr{d}} - \ddot{w}_h\right) + p_2\left(\dddot{\mathscr{d}} - \dddot{w}_h\right)\\
&\quad - \left(\ddot{\not{f}}_c\xi_1 + 3\ddot{\not{f}}_c\dot{\xi}_1 + 3\ddot{\not{f}}_c\ddot{\xi}_1 + \not{f}_c\dddot{\xi}_1\right)\mathcal{U} - 3\left(\ddot{\not{f}}_c\xi_1 + 2\ddot{\not{f}}_c\dot{\xi}_1 + \not{f}_c\ddot{\xi}_1\right)\dot{\mathcal{U}} - 3\left(\ddot{\not{f}}_c\xi_1 + \not{f}_c\dot{\xi}_1\right)\ddot{\mathcal{U}} - \not{f}_c\xi_1\dddot{\mathcal{U}},\\
\overset{(4)}{p}_2 &= \ddot{p}_1\left(w_h - \mathscr{d}\right) + 3\dot{p}_1\left(\dot{w}_h - \dot{\mathscr{d}}\right) + 3\dot{p}_1\left(\ddot{w}_h - \ddot{\mathscr{d}}\right) + p_1\left(\dddot{w}_h - \dddot{\mathscr{d}}\right)\\
&\quad + \left(\ddot{\not{f}}_c\xi_2 + 3\ddot{\not{f}}_c\dot{\xi}_2 + 3\ddot{\not{f}}_c\ddot{\xi}_2 + \not{f}_c\dddot{\xi}_2\right)\mathcal{U} + 3\left(\ddot{\not{f}}_c\xi_2 + 2\ddot{\not{f}}_c\dot{\xi}_2 + \not{f}_c\ddot{\xi}_2\right)\dot{\mathcal{U}} + 3\left(\ddot{\not{f}}_c\xi_2 + \not{f}_c\dot{\xi}_2\right)\ddot{\mathcal{U}} + \not{f}_c\xi_2\dddot{\mathcal{U}},\\
\overset{(4)}{\mathcal{L}} &= \dddot{\mathscr{d}} - \dddot{w}_h - \left(\ddot{\not{f}}_c\Gamma + 3\ddot{\not{f}}_c\dot{\Gamma} + 3\ddot{\not{f}}_c\ddot{\Gamma} + \not{f}_c\dddot{\Gamma}\right)\mathcal{U} - 3\left(\ddot{\not{f}}_c\Gamma + 2\ddot{\not{f}}_c\dot{\Gamma} + \not{f}_c\ddot{\Gamma}\right)\dot{\mathcal{U}} - 3\left(\ddot{\not{f}}_c\Gamma + \not{f}_c\dot{\Gamma}\right)\ddot{\mathcal{U}} - \not{f}_c\Gamma\dddot{\mathcal{U}}.
\end{aligned} \tag{A.24}$$

All the elements that appear in Eq. (A.24) are computed with the following formulation. The third time derivative of $\hat{z}$ is:

$$\begin{aligned}
\dddot{\hat{z}} &= \dddot{\mathcal{C}}\not{f}_{\mathcal{D}} + 3\ddot{\mathcal{C}}\dot{\not{f}}_{\mathcal{D}} + 3\dot{\mathcal{C}}\ddot{\not{f}}_{\mathcal{D}} + \mathcal{C}\dddot{\not{f}}_{\mathcal{D}}, \quad \dddot{\mathcal{C}} = 2\left(\dddot{Y}q_2 + 3\ddot{Y}\dot{q}_2 + 3\dot{Y}\ddot{q}_2 + Y\overset{(3)}{q}_2 - \dddot{X}q_1 - 3\ddot{X}\dot{q}_1 - 3\dot{X}\ddot{q}_1 - X\overset{(3)}{q}_1\right),\\
\dddot{\mathcal{D}} &= \dddot{r}q_s + 3\ddot{r}\dot{q}_s + 3\dot{r}\ddot{q}_s + r\overset{(3)}{q}_s, \quad \overset{(3)}{q}_s = 2\left(3\dot{q}_1\ddot{q}_1 + q_1\overset{(3)}{q}_1 + 3\dot{q}_2\ddot{q}_2 + q_2\overset{(3)}{q}_2\right).
\end{aligned} \tag{A.25}$$

The third order time derivatives of X and Y are computed in:

$$\begin{aligned}
\dddot{X} &= \dddot{r}\,c_L + 2\ddot{r}\dot{c}_L + \dot{r}\ddot{c}_L - \dddot{\omega}\vartheta_L - 2\ddot{\omega}\dot{\vartheta}_L - \omega\ddot{\vartheta}_L,\\
\dddot{Y} &= \dddot{r}\,\vartheta_L + 2\ddot{r}\dot{\vartheta}_L + \dot{r}\ddot{\vartheta}_L + \dddot{\omega}c_L + 2\ddot{\omega}\dot{c}_L + \omega\ddot{c}_L,\\
\dddot{\omega} &= \dddot{h}\not{f}_r + 2\ddot{h}\dot{\not{f}}_r + h\ddot{\not{f}}_r,\\
\dddot{r} &= \mu\left(\dddot{\not{f}}_c r_{pl} + 2\ddot{\not{f}}_c\dot{r}_{pl} + \dot{\not{f}}_c\ddot{r}_{pl}\right),\\
\dddot{r}_{pl} &= \dddot{p}_2\vartheta_L + 2\ddot{p}_2\dot{\vartheta}_L + p_2\ddot{\vartheta}_L - \dddot{p}_1 c_L - 2\ddot{p}_1\dot{c}_L - p_1\ddot{c}_L.
\end{aligned} \tag{A.26}$$

The third order time derivative of $\mathcal{U}$ and U_z can be computed with:

$$\begin{aligned}
\dddot{\mathcal{U}} &= -A\left(\overset{(3)}{U}_z\not{f}_{r^3} + 3\ddot{U}_z\dot{\not{f}}_{r^3} + 3\dot{U}_z\ddot{\not{f}}_{r^3} + U_z\overset{(3)}{\not{f}}_{r^3}\right),\\
\overset{(3)}{U}_z &= -6\left(3\dot{\hat{z}}\ddot{\hat{z}} + \hat{z}\,\overset{(3)}{\hat{z}}\right),\\
\frac{d^3(r^3)}{dt^3} &= \overset{(3)}{r}_c = 3(2\dot{r}^3 + 6r\dot{r}\ddot{r} + r^2\,\overset{(3)}{r}).
\end{aligned} \tag{A.27}$$

The third order derivatives of Γ and β are:

$$\begin{aligned}
\dddot{\Gamma} &= \overset{(3)}{\not{f}}_{\alpha} + \dddot{\alpha}\left(1 - \frac{r}{a}\right) - 3\ddot{\alpha}\frac{\dot{r}}{a} - 3\dot{\alpha}\frac{\ddot{r}}{a} - \alpha\frac{\dddot{r}}{a}, \quad \dddot{\alpha} = \overset{(3)}{\not{f}}_{1+\beta},\\
\dddot{\beta} &= -\tfrac{1}{2}\left(\dddot{p}\not{f}_{\beta} + 2\ddot{p}_s\dot{\not{f}}_{\beta} + \dot{p}_s\ddot{\not{f}}_{\beta}\right), \overset{(3)}{\not{f}}_{\beta}, \quad \dddot{p}_s = 2\left(3\dot{p}_1\ddot{p}_1 + p_1\overset{(3)}{p}_1 + 3\dot{p}_2\ddot{p}_2 + p_2\overset{(3)}{p}_2\right).
\end{aligned} \tag{A.28}$$

The third order time derivative of I is computed from the next expressions:

$$\begin{aligned}
\dddot{I} &= 3A\left[\left(\dddot{\hat{z}}\,\delta + 3\ddot{\hat{z}}\dot{\delta} + 3\dot{\hat{z}}\ddot{\delta} + \hat{z}\,\dddot{\delta}\right)\not{f}_{h} + 3\left(\ddot{\hat{z}}\delta + 2\dot{\hat{z}}\dot{\delta} + \hat{z}\ddot{\delta}\right)\dot{\not{f}}_{h} + 3\left(\dot{\hat{z}}\delta + \hat{z}\dot{\delta}\right)\ddot{\not{f}}_{h} + \hat{z}\delta\dddot{\not{f}}_{h}\right],\\
\dddot{h} &= \dddot{h}r_c + 3\ddot{h}\dot{r}_c + 3\dot{h}\ddot{r}_c + h\,\overset{(3)}{r}_c,\\
\dddot{h} &= \left(\dddot{g}_c - 2\dddot{g}_r\mathcal{U} - 6\ddot{g}_r\dot{\mathcal{U}} - 6\dot{g}_r\ddot{\mathcal{U}} - r^2\dddot{\mathcal{U}}\right)\not{f}_h + 2\left(\ddot{g}_c - 2\ddot{g}_r\mathcal{U} - 4\dot{g}_r\dot{\mathcal{U}} - r^2\ddot{\mathcal{U}}\right)\dot{\not{f}}_h + \left(\dot{g}_c - 2\dot{g}_r\mathcal{U} - r^2\dot{\mathcal{U}}\right)\ddot{\not{f}}_h,\\
\dddot{c} &= \left(\frac{\mu^2}{\nu}\right)^{1/3}\dddot{\beta},\\
\dddot{\delta} &= -\overset{(3)}{q}_s.
\end{aligned} \tag{A.29}$$

The third time derivative of $\mathscr{d}$ is:

$$\dddot{\mathscr{d}} = \left(\dddot{h} - \dddot{c}\right)\not{f}_{r^2} + 3\left(\ddot{h} - \ddot{c}\right)\dot{\not{f}}_{r^2} + 3\left(\dot{h} - \dot{c}\right)\ddot{\not{f}}_{r^2} + (h - c)\overset{(3)}{\not{f}}_{r^2}, \quad \frac{d^3(r^2)}{dt^3} = \overset{(3)}{r}_s = 2\overset{(3)}{g}_r. \tag{A.30}$$

The third order time derivatives of $w_h, \xi_1, \xi_2, \vartheta_L$ and c_L are given by:

$$\begin{aligned}
\overset{(3)}{w}_h &= \dddot{I}\,\hat{z} + 3\ddot{I}\dot{\hat{z}} + 3\dot{I}\ddot{\hat{z}} + I\,\overset{(3)}{\hat{z}},\\
\overset{(3)}{\xi}_1 &= \frac{\dddot{X}}{a} + 2\overset{(3)}{p}_2,\\
\overset{(3)}{\xi}_2 &= \frac{\dddot{Y}}{a} + 2\overset{(3)}{p}_1,\\
\overset{(3)}{\vartheta}_L &= \dddot{Y}\not{f}_r + 3\ddot{Y}\dot{\not{f}}_r + 3\dot{Y}\ddot{\not{f}}_r + Y\overset{(3)}{\not{f}}_r,\\
\overset{(3)}{c}_L &= \dddot{X}\not{f}_r + 3\ddot{X}\dot{\not{f}}_r + 3\dot{X}\ddot{\not{f}}_r + X\overset{(3)}{\not{f}}_r.
\end{aligned} \tag{A.31}$$

A.5. Derivatives of the $\not{f}_{\vartheta}$ and g_s time derivatives with respect to the element x

When $\overset{(k)}{\not{f}}_s$ is derived with respect to x, then all the derivatives up to $\overset{(k)}{s}$ with respect to x (with standard notation $\overset{(k)}{s}_x$) are needed (or up to $\overset{(k+1)}{s}$ in the case of $\overset{(k)}{g}_s$). The notation for the cross derivative used here meets $\partial\overset{(k)}{\not{f}}_s/\partial x = \overset{(k),x}{\not{f}}_s$, chose on purpose for the compact expressions developed in this appendix section.

Thus, the function that computes $\overset{(k),x}{\underset{s}{\mathscr{f}}}$ needs not only the vector $\left[s,\dot{s},\cdots,\overset{(k)}{s}\right]$, but also $\left[s_x,\dot{s}_x,\cdots,\overset{(k)}{\underset{x}{s}}\right]$ as input. Here are the expressions of the function that implements these derivatives:

$$\begin{aligned}
\frac{\partial \mathscr{f}_s}{\partial x} &= \overset{x}{\underset{s}{\mathscr{f}}} = && -\frac{s_x}{s^2},\\
\frac{\partial \dot{\mathscr{f}}_s}{\partial x} &= \overset{(1),x}{\underset{s}{\mathscr{f}}} = && -\frac{\dot{s}_x}{s^2}+2\frac{\dot{s}s_x}{s^3},\\
\frac{\partial \ddot{\mathscr{f}}_s}{\partial x} &= \overset{(2),x}{\underset{s}{\mathscr{f}}} = && -\frac{\ddot{s}_x}{s^2}+2\frac{\ddot{s}s_x+2\dot{s}\dot{s}_x}{s^3}-6\frac{\dot{s}^2 s_x}{s^4},\\
\frac{\partial \overset{(3)}{\mathscr{f}}_s}{\partial x} &= \overset{(3),x}{\underset{s}{\mathscr{f}}} = && -\frac{\overset{(3)}{s}_x}{s^2}+2\frac{\ddot{s}s_x+3(\dot{s}_x\dot{s}+\ddot{s}\dot{s}_x)}{s^3}-18\frac{\ddot{s}\dot{s}s_x+\dot{s}^2\dot{s}_x}{s^4}+24\frac{\dot{s}^3 s_x}{s^5},\\
\frac{\partial \overset{(4)}{\mathscr{f}}_s}{\partial x} &= \overset{(4),x}{\underset{s}{\mathscr{f}}} = && -\frac{\overset{(4)}{s}_x}{s^2}+2\frac{\overset{(4)}{s}s_x+6\ddot{s}\dot{s}_x+4\left(\ddot{s}\dot{s}+\dot{s}\overset{(3)}{s}_x\right)}{s^3}-6\frac{\overset{(3)}{s}\dot{s}s_x+6\left(2\dot{s}\dot{s}_x\ddot{s}+\dot{s}^2\ddot{s}_x\right)+3\ddot{s}^2 s_x}{s^4}\\
& && +12\frac{12\dot{s}^2\ddot{s}s_x-8\dot{s}^3\dot{s}_x}{s^5}+120\frac{\dot{s}^4 s_x}{s^6}.
\end{aligned} \tag{A.32}$$

And similarly for $\overset{(k),x}{\underset{s}{\mathscr{g}}}$ the derivatives are:

$$\begin{aligned}
\frac{\partial g_s}{\partial x} &= \overset{x}{\underset{s}{\mathscr{g}}} = && s_x\dot{s}+s\dot{s}_x,\\
\frac{\partial \dot{g}_s}{\partial x} &= \overset{(1),x}{\underset{s}{\mathscr{g}}} = && 2\dot{s}\dot{s}_x+s_x\ddot{s}+s\ddot{s}_x,\\
\frac{\partial \ddot{g}_s}{\partial x} &= \overset{(2),x}{\underset{s}{\mathscr{g}}} = && 3\dot{s}_x\ddot{s}+3\dot{s}\ddot{s}_x+s_x\overset{(3)}{s}+s\overset{(3)}{\underset{x}{s}},\\
\frac{\partial \overset{(3)}{g}_s}{\partial x} &= \overset{(3),x}{\underset{s}{\mathscr{g}}} = && 6\ddot{s}\ddot{s}_x+4\dot{s}_x\overset{(3)}{s}+4\dot{s}\overset{(3)}{\underset{x}{s}}+s_x\overset{(4)}{s}+s\overset{(4)}{\underset{x}{s}},\\
\frac{\partial \overset{(4)}{g}_s}{\partial x} &= \overset{(4),x}{\underset{s}{\mathscr{g}}} = && 10\ddot{s}_x\overset{(3)}{s}+10\ddot{s}\overset{(3)}{\underset{x}{s}}+5\dot{s}_x\overset{(4)}{s}+5\dot{s}\overset{(4)}{\underset{x}{s}}+s_x\overset{(5)}{s}+s\overset{(5)}{\underset{x}{s}}.
\end{aligned} \tag{A.33}$$

A.6. Derivatives of inclination and right ascension of the ascending node

Consider the specific angular momentum as the cross product of position and velocity both given in an inertial frame (I), $\boldsymbol{h}=\boldsymbol{r}\times\boldsymbol{v}$. The inclination i can be computed as a function of $\boldsymbol{r}$ and $\boldsymbol{v}$ from:

$$h=(\boldsymbol{h}^{\mathsf{T}}\boldsymbol{h})^{1/2},\qquad h_z=\boldsymbol{k}^{\mathsf{T}}\boldsymbol{h},\qquad i=\arccos\left(\frac{h_z}{h}\right). \tag{A.34}$$

The right ascension of the ascending node Ω is computed from:

$$\begin{aligned}
&\boldsymbol{n}^*=\boldsymbol{k}\times\boldsymbol{h},\qquad n^*=(\boldsymbol{n}^{*\mathsf{T}}\boldsymbol{n}^*)^{1/2},\\
&\boldsymbol{n}=\frac{\boldsymbol{n}^*}{n^*},\qquad \Omega=\arccos(\boldsymbol{i}^{\mathsf{T}}\boldsymbol{n}).
\end{aligned} \tag{A.35}$$

For the derivation of i and Ω with respect to position and velocity let us first define the cross product of a $3\times n$ matrix M by a 3×1 vector $\boldsymbol{d}$ as the cross product of each column in M by $\boldsymbol{d}$. This means that the *i-eth* column of $\mathrm{D}=\mathrm{M}\times\boldsymbol{d}$ meets $\mathrm{D}_i=\mathrm{M}_i\times\boldsymbol{d}$. In other words, the cross product of matrix and vector acts column-wise for the next derivation. The differentiation with respect to the state for the inclination observable results in the following:

$$\begin{aligned}
&\frac{\partial \boldsymbol{h}}{\partial \boldsymbol{r}}=\frac{\partial \boldsymbol{r}}{\partial \boldsymbol{r}}\times\boldsymbol{v}+\boldsymbol{r}\times\frac{\partial \boldsymbol{v}}{\partial \boldsymbol{r}}=I\times\boldsymbol{v},\\
&\frac{\partial \boldsymbol{h}}{\partial \boldsymbol{v}}=\frac{\partial \boldsymbol{r}}{\partial \boldsymbol{v}}\times\boldsymbol{v}+\boldsymbol{r}\times\frac{\partial \boldsymbol{v}}{\partial \boldsymbol{v}}=-I\times\boldsymbol{r},\\
&\frac{\partial \boldsymbol{h}}{\partial \boldsymbol{y}}=\left[\frac{\partial \boldsymbol{h}}{\partial \boldsymbol{r}},\frac{\partial \boldsymbol{h}}{\partial \boldsymbol{v}}\right],\\
&\frac{\partial h_z}{\partial \boldsymbol{y}}=\boldsymbol{e}_3^{\mathsf{T}}\frac{\partial \boldsymbol{h}}{\partial \boldsymbol{y}},\\
&\frac{\partial h}{\partial \boldsymbol{y}}=\frac{\boldsymbol{h}^{\mathsf{T}}}{h}\frac{\partial \boldsymbol{h}}{\partial \boldsymbol{y}},\\
&\frac{\partial i}{\partial \boldsymbol{y}}=-\frac{1}{\sqrt{1-\cos^2 i}}\left[\frac{\partial h_z}{\partial \boldsymbol{y}}-\cos i\frac{\partial h}{\partial \boldsymbol{y}}\right]\frac{1}{h}.
\end{aligned}$$

For the right ascension of the ascending node on the other hand:

$$\begin{aligned}
&\frac{\partial \boldsymbol{n}^*}{\partial \boldsymbol{y}}=\boldsymbol{e}_3\times\frac{\partial h}{\partial \boldsymbol{y}}=-\frac{\partial h}{\partial \boldsymbol{y}}\times\boldsymbol{e}_3,\\
&\frac{\partial n^*}{\partial \boldsymbol{y}}=\frac{\boldsymbol{n}^{*\mathsf{T}}}{n^*}\frac{\partial \boldsymbol{n}^*}{\partial \boldsymbol{y}},\\
&\frac{\partial \boldsymbol{n}}{\partial \boldsymbol{y}}=\left[\frac{\partial \boldsymbol{n}^*}{\partial \boldsymbol{y}}-\boldsymbol{n}\frac{\partial n^*}{\partial \boldsymbol{y}}\right]\frac{1}{n^*},\\
&\frac{\partial \Omega}{\partial \boldsymbol{y}}=-\frac{1}{\sqrt{1+\cos^2\Omega}}\boldsymbol{e}_1^{\mathsf{T}}\frac{\partial \boldsymbol{n}}{\partial \boldsymbol{y}}.
\end{aligned}$$

A.7. Generalized equinoctial orbital elements auxiliary functions

Algorithms 1 and 2 are basic conversion functions needed to work with the generalized equinoctial orbital elements.

Algorithm 1. $\boldsymbol{\chi}=[\upsilon\, p_1\, p_2\, q_1\, q_2\, \mathcal{L}]^{\mathsf{T}}=\mathrm{RV2GEQOE}_{fun}(\boldsymbol{r}\rfloor_{ECI},\boldsymbol{v}\rfloor_{ECI},\mu,J_2,R_\oplus)$

1: $r=\|\boldsymbol{r}\|,\quad \upsilon=\|\boldsymbol{v}\|$
2: $\boldsymbol{h}=\boldsymbol{r}\times\boldsymbol{v},\ h=\|\boldsymbol{h}\|,\dot{r}=\frac{\boldsymbol{r}\cdot\boldsymbol{v}}{r}$
3: $\hat{z}=\boldsymbol{r}(3)/r$
4: $A=\frac{\mu J_2 R_\oplus^2}{2},\mathcal{U}=-\frac{A}{r^3}(1-3\hat{z}^2),\mathcal{U}_{\mathrm{eff}}=\frac{h^2}{2r^2}+\mathcal{U}$
5: $\boldsymbol{e}_r=\boldsymbol{r}/r,\boldsymbol{e}_h=\boldsymbol{h}/h,\boldsymbol{e}_f=\boldsymbol{e}_h\times\boldsymbol{e}_r$
6: $\boldsymbol{e}_x=[1,0,0]^{\mathsf{T}},\boldsymbol{e}_y=[0,1,0]^{\mathsf{T}},\boldsymbol{e}_z=[0,0,1]^{\mathsf{T}}$
7: **Total energy:** $\varepsilon=\varepsilon_K+\mathcal{U}=\frac{\upsilon^2}{2}-\frac{\mu}{r}+\mathcal{U}$
8: **Generalized mean motion:** $\nu=\frac{1}{\mu}(-2\varepsilon)^{3/2}$
9: $q_1=\frac{e_h\dot{e}_x}{1+e_h\dot{e}_z},q_2=\frac{-e_h\dot{e}_x}{1+e_h\dot{e}_z}$
10: $\boldsymbol{e}_X=\frac{1}{1+q_1^2+q_2^2}\left[1-q_1^2+q_2^2,2q_1q_2,-2q_1\right]^{\mathsf{T}}$
11: $\boldsymbol{e}_Y=\frac{1}{1+q_1^2+q_2^2}\left[2q_1q_2,1+q_1^2-q_2^2,2q_2\right]^{\mathsf{T}}$
12: **Generalized angular momentum:** $c=\sqrt{2r^2\mathcal{U}_{\mathrm{eff}}}$
13: **Generalized velocity vector:** $\upsilon=\dot{r}\boldsymbol{e}_r+\frac{c}{r}\boldsymbol{e}_f$
14: **Generalized eccentricity vector:** $\boldsymbol{g}=\frac{1}{\mu}\upsilon(\boldsymbol{r}\times\upsilon)-\boldsymbol{e}_r$
15: $p_1=\boldsymbol{g}\cdot\boldsymbol{e}_Y,p_2=\boldsymbol{g}\cdot\boldsymbol{e}_X$
16: $X=\boldsymbol{r}\cdot\boldsymbol{e}_X,Y=\boldsymbol{r}\cdot\boldsymbol{e}_Y$
17: $\beta=\sqrt{1-p1^2-p_2^2},\alpha=\frac{1}{1+\beta}$
18: **Generalized semi-major axis:** $a=-\frac{\mu}{2\varepsilon}=\left(\frac{\mu}{\nu^2}\right)^{1/3}$
19: $\cos\mathcal{K}=p_2+\frac{1}{a\beta}\left[(1-\alpha p_2^2)X-\alpha p_1p_2Y\right]$
20: $\sin\mathcal{K}=p_1+\frac{1}{a\beta}\left[(1-\alpha p_1^2)Y-\alpha p_1p_2X\right]$
21: $\mathcal{L}=\mathrm{atan2}(\sin\mathcal{K},\cos\mathcal{K})+\frac{1}{a\beta}(Xp_1-Yp_2)$

Algorithm 2. $X\rfloor_{ECI} = [\boldsymbol{r}^\intercal, \boldsymbol{v}^\intercal]^\intercal = \text{GEQOE2RV}_{fun}(v, p_1, p_2, q_1, q_2, \mathcal{L}, \mu, \text{J}_2, R_\oplus)$

Numerically solve Kepler's equation: $\mathcal{K} \leftarrow \mathcal{L} = \mathcal{K} + p_1 \cos\mathcal{K} - p_2 \sin\mathcal{K}$

$\boldsymbol{e}_X = \frac{1}{1+q_1^2+q_2^2}\left[1 - q_1^2 + q_2^2, 2q_1q_2, -2q_1\right]^\intercal$

$\boldsymbol{e}_Y = \frac{1}{1+q_1^2+q_2^2}\left[2q_1q_2, 1 + q_1^2 - q_2^2, 2q_2\right]^\intercal$

$\beta = \sqrt{1 - p1^2 - p_2^2}, \alpha = \frac{1}{1+\beta}$

$a = \left(\frac{\mu}{v^2}\right)^{1/3}$

$X = a\left[\alpha p_1 p_2 \sin\mathcal{K} + (1 - \alpha p_1^2)\cos\mathcal{K} - p_2\right]$

$Y = a\left[\alpha p_1 p_2 \cos\mathcal{K} + (1 - \alpha p_2^2)\sin\mathcal{K} - p_1\right]$

$\boldsymbol{r} = X\boldsymbol{e}_X + Y\boldsymbol{e}_Y$

$r = a(1 - p_1 \sin\mathcal{K} - p_2 \cos\mathcal{K})$

$\hat{z} = \boldsymbol{r}(3)/r$

$A = \frac{\mu \text{J}_2 R_\oplus^2}{2}, \mathcal{U} = -\frac{A}{r^3}(1 - 3\hat{z}^2)$

$\dot{r} = \frac{\sqrt{\mu a}}{r}(p_2 \sin\mathcal{K} - p_1 \cos\mathcal{K})$

$\cos L = \frac{X}{r}, \sin L = \frac{Y}{r}$

$c = \left(\frac{\mu^2}{v}\right)^{1/3}\sqrt{1 - q_1^2 - q_2^2}, h = \sqrt{c^2 - 2r^2\mathcal{U}}$

$\dot{X} = \dot{r}\cos L - \frac{h}{r}\sin L$

$\dot{Y} = \dot{r}\sin L + \frac{h}{r}\cos L$

$\boldsymbol{v} = \dot{X}\boldsymbol{e}_X + \dot{Y}\boldsymbol{e}_Y$

References

Amato, D., Bombardelli, C., Baù, G., et al., 2019. Non-averaged regularized formulations as an alternative to semi-analytical orbit propagation methods. Celest. Mech. Dynam. Astron. 131, 1–38.

Baù, G., Hernando-Ayuso, J., Bombardelli, C., 2021. A generalization of the equinoctial orbital elements. Celest. Mech. Dynam. Astron. 133, 1–29.

Broucke, R.A., Cefola, P.J., 1972. On the equinoctial orbit elements. Celest. Mech. 5 (3), 303–310.

Bruinsma, S., Thuillier, G., Barlier, F., 2003. The DTM-2000 empirical thermosphere model with new data assimilation and constraints at lower boundary: accuracy and properties. J. Atmos. Solar-terrestrial Phys. 65 (9), 1053–1070.

DeMars, K.J., Jah, M.K., Schumacher, P.W., 2012. Initial orbit determination using short-arc angle and angle rate data. IEEE Trans. Aerosp. Electron. Syst. 48 (3), 2628–2637.

ESA (2023). ESA's space environment report 2023. URL: https://www.esa.int/Space_Safety/ESA_s_Space_Environment_Report_2023 accessed: 2024-01-10.

Escobal, P., 1970. Methods of orbit determination. Krieger Pub Co..

Goff, G.M. (2015). Orbit Estimation of Non-Cooperative Maneuvering Spacecraft. Ph.D. thesis Air Force Institute of Technology. URL: https://scholar.afit.edu/etd/202/.

Gomez, R., Salmerón, J.M.-V., Besso, P., et al., 2019. Initial operations of the breakthrough Spanish Space Surveillance and Tracking Radar (S3TSR) in the European context. In: In 1st ESA NEO and Debris Detection Conference. Presented paper. Darmstadt, Germany, URL: https://conference.sdo.esoc.esa.int/proceedings/neosst1/paper/479.

Gooding, R., 1993. A new procedure for orbit determination based on three lines of sight (angles only). Defence Research Agency Farnborough, UK.

Hatten, N., Russell, R.P., 2017. A smooth and robust Harris-Priester atmospheric density model for low Earth orbit applications. Adv. Space Res. 59 (2), 571–586.

Hernando-Ayuso, J., Bombardelli, C., Baù, G., et al., 2023. Near-linear orbit uncertainty propagation using the generalized equinoctial orbital elements. J. Guid., Control, Dynam. 46 (4), 654–665.

Kaushik, A.S. (2016). A statistical comparison between Gibbs and Herrick-Gibbs orbit determination methods. Ph.D. thesis.

Long, A.C., Cappellari Jr, J., Velez, C., et al., 1989. Goddard trajectory determination system (GTDS) mathematical theory (revision 1). National Aeronautics and Space Administration/Goddard Space Flight Center, FDD/552-89/001 and CSC/TR-89/6001.

Ma, H., Baù, G., Bracali Cioci, D., et al., 2018. Preliminary orbits with line-of-sight correction for leo satellites observed with radar. Celest. Mech. Dynam. Astron. 130 (10), 70.

Maisonobe, L., Pommier, V., Parraud, P., 2010. Orekit: An open source library for operational flight dynamics applications. In: In 4th international conference on astrodynamics tools and techniques. European Space Agency Paris, pp. 3–6.

Martinusi, V., Dell'Elce, L., Kerschen, G., 2015. Analytic propagation of near-circular satellite orbits in the atmosphere of an oblate planet. Celest. Mech. Dynam. Astron. 123, 85–103.

Milani, A., Gronchi, G.F., Knežević, Z., et al., 2005. Orbit determination with very short arcs: II. identifications. Icarus 179 (2), 350–374.

Milani, A., Gronchi, G.F., Vitturi, M.D.M., et al., 2004. Orbit determination with very short arcs. I admissible regions. Celest. Mech. Dynam. Astron. 90, 57–85.

Montilla, J.M., Sanchez, J.C., Vazquez, R., et al., 2023a. Manoeuvre detection in Low Earth Orbit with radar data. Adv. Space Res. 72 (7), 2689–2709.

Montilla, J.M., Vazquez, R., & Di Lizia, P. (2023b). Mixture-based cost metrics for maneuver detection using radar track data. In 33rd AAS/AIAA Space Flight Mechanics Meeting AAS 23–267 (pp. 1–16).

Pastor, A., Sanjurjo-Rivo, M., Escobar, D., 2021. Initial orbit determination methods for track-to-track association. Adv. Space Res. 68 (7), 2677–2694.

Picone, J., Hedin, A., Drob, D.P., et al., 2002. NRLMSISE-00 empirical model of the atmosphere: Statistical comparisons and scientific issues. J. Geophys. Res.: Space Phys. 107 (A12), SIA-15.

Reihs, B., Vananti, A., Schildknecht, T., et al., 2021. Application of attributables to the correlation of surveillance radar measurements. Acta Astronaut. 182, 399–415.

Schutz, B., Tapley, B., Born, G.H., 2004. Statistical orbit determination. Elsevier.

Shang, H., Chen, D., Cao, H., et al., 2018. Initial orbit determination using very short arc data based on double-station observation. IEEE Trans. Aerosp. Electron. Syst. 55 (4), 1596–1611.

Siminski, J. (2016). Techniques for assessing space object cataloguing performance during design of surveillance systems. In 6th International Conference on Astrodynamics Tools and Techniques (ICATT) (pp. 14–17).

Tao, X., Li, Z., Gong, Q., et al., 2020. Uncertainty analysis of the short-arc initial orbit determination. IEEE Access 8, 38045–38059.

Vallado, D.A., 2001. Fundamentals of astrodynamics and applications, volume 12. Springer Science & Business Media.

Vallado, D.A., Carter, S.S., 1998. Accurate orbit determination from short-arc dense observational data. J. Astronaut. Sci. 46, 195–213.

Vananti, A., Schildknecht, T., Siminski, J. et al. (2017). Tracklet-tracklet correlation method for radar and angle observations. In 7th European Conference on Space Debris. ESOC Darmstadt volume 4.

Zhang, S., Fu, T., Chen, D., et al., 2019. An initial orbit determination method using single-site very short arc radar observations. IEEE Trans. Aerosp. Electron. Syst. 56 (3), 1856–1872.